Bayesian inference of subglacial channel structures from water-pressure and tracer-transit-time data: A numerical study based on a 2-D geostatistical modelling approach

Inigo Irarrazaval[1], Mauro A. Werder[2], Niklas Linde[3], James Irving[3], Frederic Herman[1], Gregoire Mariethoz[1].

[1]University of Lausanne, Faculty of Geosciences, Institute of Earth Surface Dynamics.

[2]ETH Zurich, Hydrology and Glaciology (VAW), Laboratory of Hydraulics.

[3]University of Lausanne, Faculty of Geosciences, Institute of Earth Sciences.

Corresponding author: Inigo Irarrazaval (inigo.irarrazavalbustos@unil.ch)

Key points

- Subglacial drainage networks are modeled in two dimensions through a combination of physical and geostatistical methods.
- Bayesian inference is used to retrieve channel networks that honor water pressure and tracer-transit times within a framework of uncertainty.
- Expected channel network physical characteristics are captured for each water recharge scenario.

Abstract

Characterizing subglacial water flow is critical for understanding basal sliding and processes occurring under glaciers and ice sheets. Development of subglacial numerical models as well as acquisition of water pressure and tracer data have provided valuable insights into subglacial systems and their evolution. Despite these advances, numerical models, data conditioning and uncertainty quantification are difficult, principally due to high number of unknown parameters and expensive forward computations. In this study, we aim to infer the properties of a subglacial drainage system in two dimensions using a framework that combines physical and geostatistical processes. The methodology is composed of three main components: (i) a channel generator to produce networks of the subglacial system; (ii) a physical model that computes pressure and mass transport in steady state; and (iii) Bayesian inversion in which the outputs (pressure, tracer-transit times) are compared with synthetic data, thus allowing for parameter estimation and uncertainty quantification. We evaluate the ability of this framework to infer the subglacial characteristics of a synthetic ice sheet produced by a physically-complex deterministic model, under different recharge scenarios. Results show that our methodology captures expected physical characteristics for each meltwater supply condition, while the precise locations of channels remain difficult to constrain. The framework enables uncertainty quantification and the results highlight its potential to infer properties of real subglacial systems using observed water pressure and tracer-transit times.

1 Introduction

Subglacial water flow processes, which take place at the base of glaciers and ice sheets, play a crucial role in ice flow dynamics [e.g.: *Cuffey and Paterson*, 2010; *Iken*, 1981], bedrock erosion [e.g.: *Herman et al.*, 2011; *Koppes et al.*, 2015], catchment hydrology [e.g.: *Verbunt et al.*, 2003], and potential hazards such as glacial outburst floods [e.g.: *Huss et al.*, 2007]. As climate change occurs, temperature and precipitation patterns are altered, which affects glacier dynamics, with ultimately wide-ranging consequences such as a reduction of fresh water storage and sea level rise [e.g.: *Benn and Evans*, 2010]. The processes that occur at the ice-bedrock interface are still poorly understood because of the difficulty to observe and quantify subglacial systems.

Subglacial hydrological systems have been conceptualized as a combination of two main types of drainage systems: a distributed slow system and a channelized efficient system [*Fountain and Walder*, 1998]. Distributed slow drainage can occur as a water sheet or film flow [*Weertman*, 1972], as flow through linked cavities [*Kamb*, 1987; *Walder*, 1986], or through permeable sediments, while efficient drainage corresponds to a fast-flowing channel network formed during periods of high discharge. Channelized drainage occurs either through conduits melted into the base of the ice, known as Röthlisberger (R) channels [*Röthlisberger*, 1972], or through channels incised into the bedrock or sediments [e.g.: *Nye*, 1976]. It is recognized that channels are often formed by a combination of ice melting and sediment/bedrock incision [*Gulley et al.*, 2014]. The relative contribution of the distributed versus channelized systems has a strong impact on the distribution of water pressure in subglacial systems. During winter, low water fluxes at the glacier bed combined with ice creep result in channel closure. Consequently, the late-winter configuration is often described as a slow and inefficient system. During spring and summer, greater amounts of meltwater imply an enlargement of the channels. During transition periods a sudden increase in meltwater discharge might surpass the capacity of the channelized system, thereby, increasing the water pressure and causing abrupt acceleration in ice motion [*Schoof*, 2010], until channels become large enough to accommodate the discharge.

Several types of data provide insights into the temporal evolution of subglacial systems [e.g.: *Gulley et al.*, 2014; *Nienow et al.*, 1996]. These include tracer-transit times measured throughout the day [e.g.: *Schuler et al.*, 2004] and at different periods of the year [e.g.: *Chandler et al.*, 2013]; water-pressure measurements in boreholes drilled into the glacier {e.g.: \Schoof, 2014 #191;Hubbard, 1995 #142;Rada, 2018 #263}; and the analysis of seismic tremor produced by water flow in the channels [*Gimbert et al.*, 2016]. Only in a few instances have scientists been able to directly access subglacial systems via moulins or crevasses to acquire direct observations in parts of the channel network [*Gulley et al.*, 2012].

As most of the above data are indirect, numerical models have been increasingly used to study subglacial systems. One of the first models, proposed by *Shreve* [1972], was based on the premise that subglacial channels follow the gradient of the hydraulic potential on the glacier bed. Recent models have included the spontaneous formation of channels and subsequent switching from a distributed to a channelized flow regime and vice versa. Channels and cavities are described such that they are able to open through wall melting or open/close by ice creep, and water flow is computed according to the Darcy-Weisbach law for turbulent flow [*Hewitt*, 2011; *Schoof*, 2010; *Werder et al.*, 2013]. While basal drainage models can reproduce many types of subglacial physical processes, they suffer from an absence of direct and independent data for calibration [*Flowers*, 2015]. Moreover, the geometry of the subglacial drainage systems is an emergent property of the modelled process when considering advanced physically based model [*Schoof*, 2010; *Werder et al.*, 2013], which makes it difficult to perform uncertainty quantification and data conditioning, chiefly because of the need for multiple repeated simulations using very time-consuming simulation tools.

Similar challenges exist when modeling karstic systems that can be seen as analogues to subglacial drainage systems [*Covington et al.*, 2012]. It is difficult to map preferential hydraulic pathways in karst systems, yet hydrogeologists have been able to improve their characterization by incorporating geostatistical methods and inversion procedures [e.g.: *Borghi et al.*, 2012; *Mariethoz et al.*, 2010; *Rongier et al.*, 2014]. Geostatistical methods aim to characterize the spatial behaviour of a variable by inferring statistical relationships in space. For example, *Borghi et al.* [2012] presented a pseudo-genetic framework to generate karst conduits in a three-dimensional regional model. At a smaller scale, *Rongier et al.* [2014] model realistic-looking karst conduits by combining the observed conduit skeleton with Gaussian random fields. One of the benefits of using geostatistical approaches compared to process-based models is that they provide structure-imitating realizations at low computational cost. While uncertainty quantification is important given the scarcity of observations, the large computing times of process-based models can quickly overwhelm computational resources as Monte-Carlo approaches require a considerable number of forward model runs [*Linde et al.*, 2015]. In this regard, combining geostatistical and inverse approaches has been successfully used for inference of conduit geometry and data conditioning in karst aquifer models [e.g.: *Borghi et al.*, 2016; *Vuilleumier et al.*, 2012]. Therefore, it is possible to distinguish two main approaches: adding complexity to physically-based models as has been the trend in subglacial hydrology; or building parsimonious geostatistical models, which offer limited physical insights but allow for practical inversion approaches that enable data conditioning and uncertainty quantification, following recent advances in karstic systems modelling. In this study, we explore the feasibility of the latter approach in a subglacial context.

The aim of this paper is to develop and test a framework to infer channel network geometr and hydraulic properties of subglacial drainage systems in two dimensions. The overall proposed strategy is to build a channel generator, which is a geostatistical tool to produce prior channel networks at low computational cost. These prior networks are evaluated against observed data using a fast steady-state water flow model. Bayesian inference allows us to retrieve the probability distribution of network parameters that are in agreement with the data. Because of the typical data scarcity in such systems, the inverse problem is underdetermined and does not have a unique solution [e.g.: *Linde et al.*, 2017; *Mosegaard and Tarantola*, 1995]. As a result, it is important to explore the model space and obtain an ensemble of parameters that honour the observations. Such a probabilistic approach is different from optimization, in which only one solution is sought and a rigorous assessment of uncertainty is often not possible. Note that, although *Brinkerhoff et al.* [2016] used a Bayesian inference framework to explore the uncertainty and covariance structure of the parameters of a spatially aggregated (1D) model for glacier hydrology, the approach presented here differs in that we perform our analysis in 2D using a model that combines physical and geostatistical approaches.

The proposed framework has three main components: 1) a geostatistical channel generator, which combines geostatistical and physical processes to create channels; 2) a steady-state water-flow and mass-transport forward model, and 3) a Bayesian inverse framework used to condition water-pressure and tracer-transit-time observations in order to provide estimates of the model parameters and their uncertainties. To test our framework, we define a synthetic ice sheet configuration under three different forcings extracted from the Subglacial Hydrology Model Intercomparison Project (SHMIP) [*De Fleurian et al.*, 2018]. To validate our model, we consider as a reference the outputs produced by GLaDS [*Werder et al.*, 2013] under identical forcing conditions. This provides a scenario in which errors and uncertainties are controlled and understood, which is necessary to test the capabilities of the approach. The GLaDS model is a physically-based model, which accounts for channel and sheet system evolution. Therefore, GLaDS outputs provide an ideal scenario to work towards an inversion of subglacial drainage systems in 2D, as we can fully access the reference channel networks for comparison, which would be impossible for real systems. Indeed, to date researchers have not fully explored or mapped subglacial system that could be used for validation. The downside of using GLaDS as a reference is that we implicitly assume that it is a good approximation of a real unobserved system. In particular, it has been shown that GLaDS is mesh-sensitive [*Werder et al.*, 2013], resulting in additional uncertainty in channel locations. Nevertheless, we believe that the mesh-dependency does not significantly affect the use of GLaDS in our case, because our framework aims to identify characteristics related to the topology of the network as a whole, rather than to match the exact location of individual channels.

2 Methodology

A specificity of our framework is that the channel network is not emerging from physical rules. Instead, it is generated with a geostatistical process that is guided by physical constraints. This allows us to produce a large number of channel models, which are thereafter used in the inversion procedure to condition the networks to available observations of borehole water pressure and tracer-transit times.

Our framework is divided into three components, which are illustrated in Figure 1. The first component corresponds to the subglacial channel network generator, which is a geostatistical tool that from a set of parameters (to be inferred) outputs a two-dimensional channel network. This component is based on Shreve's approximation [*Shreve*, 1972], considering water pressure as a function of the ice overburden pressure, and provides the likely location of channels. A radius for each channel segment is assigned based on a stream order. The second component is the subglacial drainage water flow model, in which water pressure is computed in the domain through a laminar/turbulent finite element flow model. This component receives as input the previously generated channel network and computes steady-state water pressure and tracer-travel-time. Finally, the third component is the inversion procedure, which compares the simulated water pressure and tracer-transit times with observations through a likelihood function. Depending on the computed residuals, it will propose new input parameters to the subglacial channel network generator, until convergence. Each step is described in detail in the following subsections. All constants, variables and units used in our modeling framework are summarized in Table 1.

The model is framed in a two-dimensional domain where water flows according to the fluid potential ϕ, which is the total mechanical energy per unit volume, given by

$$\phi = \phi_z + p_w \,. \tag{1}$$

Here, p_w is the water pressure, and the $\phi_z = \rho_w g B$ is the elevation potential with water density ρ_w, acceleration of gravity g, and bedrock elevation $B=B(x,y)$. The effective pressure at the ice-bedrock interface is defined as:

$$N = p_i - p_w, \qquad (2)$$

with ice overburden pressure defined by $p_i = \rho_i g H$, where ρ_i is the ice density and $H=H(x,y)$ is the ice thickness.

2.1 Subglacial channel network generator

The channel generator uses a combination of physical and geostatistical concepts to create different types of networks, modulated by six free parameters. It is based on previous studies that used Shreve's hydraulic potential [*Shreve*, 1972] and routing algorithms to determine the approximate location of the channel network [e.g.: *Arnold et al.*, 1998; *Chu et al.*, 2016; *Livingstone et al.*, 2015; *Willis et al.*, 2012]. Additionally, we incorporate a stream order rule that assigns channel radii following *Borghi et al.* [2016]. Within our inversion framework, the networks are compared with observed data using a water flow model that produces water pressure and tracer-transit times.

For the channel generator we consider Shreve's approximation, i.e., with $N = 0$. Shreve's hydraulic potential $\phi_s = \phi_s(x, y)$ is obtained by combining equations 1 and 2:

$$\phi_s = \rho_w g B + \rho_i g H. \qquad (3)$$

In this paper we add a perturbation component $\phi_R = \phi_R(x, y)$, which is a spatially correlated random field, with the aim to add variability in order to enable creation of different types of networks (equation 4). Note that ϕ_R does not represent a physical feature per se, but rather can be seen as a spatially-correlated field that accounts for preferential hydraulic pathways, such as cavities or basal crevasses that could influence the channel network structure. This term is modeled as a two-dimensional multivariate Gaussian random field ϕ_R having integral scales l_x and l_y that represent the correlation distance along each axis. As a result, the perturbed hydraulic potential ${\phi_s}^*$ becomes:

$${\phi_s}^* = \rho_w g B + \rho_i g H + \phi_R. \qquad (4)$$

Starting from equation (4), our channel generation algorithm consists of three main steps (Figure 2): (a) generate ${\phi_s}^*$ by adding a perturbation component to the hydraulic potential assuming $N = 0$; (b) compute the channel network; and (c) assign channel radii and hydraulic parameters. These steps are implemented using Matlab and several functions of the Topotoolbox 2 library [*Schwanghart and Scherler*, 2014].

In step (a) (Figure 2a), ϕ_s is computed over the domain using equation (3), and ϕ_R is generated according to the FFT-MA approach and structural deformation technique {Hu, 2000 #184;Hu, 2004 #204;Le Ravalec, 2000 #226}. For this, we select: a mean, a variance, the integral scales which measure the correlation distance in space in the x-y axis (l_x and l_y), a Gaussian covariance model and a uniform white noise or uncorrelated uniform random field. Structural deformation makes it possible to gradually vary the integral scales l_x and l_y (Figure 3). All realizations of ϕ_R rely on the same white noise, implying that the positions of the high and low features remain at similar locations regardless of l_x and l_y. Initial tests (not shown) suggested that changing the white noise for a fixed l_x and l_y did not greatly influence the overall topology of the network, whereas changing the values of l_x and l_y was found to have a strong impact on the topological structure of the network (e.g., arborescent, long parallel channels, rectangular, etc.). For example, a given set of l_x and l_y values may result in a network of long parallel channels with a well-determined sinuosity, regardless of the white noise considered (Figure 3d). Indeed, the white noise defines the location of channel turns and intersections, but not the overall topological properties of the network. Here, we aim to infer the l_x and l_y values that correctly describe the topology of the channel network, regardless of the exact position of channelized features. Once ϕ_R has been generated, we add it to the hydraulic potential to obtain the perturbed hydraulic potential $\phi_s{}^*(x,y)$, denoted $\phi_s{}^*$ for simplicity. From this point, similar to *Arnold et al.* [1998] and *Chu et al.* [2016], the hydraulic potential is treated as the digital elevation model of a subaerial catchment to obtain preferential hydraulic pathways.

In step (b) (Figure 2b), the channel network is generated. For this, $\phi_s{}^*$ is pre-processed to ensure connectivity of the channels. This is done through removing sinks by filling internally drained basins, at a later stage the routing algorithm proposes the centerline for filled flat areas. In addition, no-flow boundary conditions are imposed on the sides of the ice sheet. This is done by temporarily creating an outside boundary of higher hydraulic potential. Then, the flow direction is computed using the D8 algorithm [*O'Callaghan and Mark*, 1984]. Previous work computed Shreve's hydraulic potential up-stream or up-glacier area for each cell, in order to identify the most likely channel locations [e.g.: *Arnold et al.*, 1998; *Chu et al.*, 2016]. Here we compute the flow accumulation, which provides for each cell the sum of the up-stream water recharge (assuming steady-state and mass conservation). The water recharge is prescribed considering a distributed homogeneous water input to represent basal melt and punctual recharge for moulins. Note that for a homogeneous distributed water recharge (with no moulins) the up-stream area equals the flow accumulation normalized by the recharge input. From this point, we extract a network where the accumulated water is over a threshold (c), which is modelled as channels.

In step (c) (Figure 2c), a radius r is assigned to each channel section of the network. We assume that channel radii increase downstream and depend on a hierarchical stream order (u_i) and two parameters (a and b) to be determined during the inversion. We use a modified version of Shreve's stream order [*Borghi et al.*, 2016; *Shreve*, 1966], where the upper branches are first given a number equal to the accumulated flow at this point. Then, the stream order is computed downstream by adding the accumulated flow from tributaries (Figure 2c). Finally, u_i is normalized by dividing all values by the highest accumulated value (the lowest channel section). Once the stream order u_i has been obtained, parameters a and b are used to transform the stream order into a channel radius using equation (5), where a is a linear scaling factor, and b controls the relative difference between the radii upstream and downstream:

$$r(u_i) = ae^{u_i b}. \tag{5}$$

Additionally, a rejection rule is introduced to avoid channel radii larger than a maximum value, which is not deemed realistic. In this study we use a maximum of 15 m. Furthermore, a transmissivity value T_d is assigned to the distributed system, which is represented as a homogeneous layer. To finish, a finite element mesh is generated that represents the distributed and channelized systems. It consists of a set of 2D quadrangular elements representing the distributed system and whose corners are the black dots in Figure 1c. Using the shared nodes (white dots in Figure 1c), an additional set of 1D elements is generated which represents the channelized system. The nodes that are in common between channelized and distributed systems ensure that both systems behave in a coupled way.

The approach described above enables generating a variety of channel networks presenting different geometric and hydraulic characteristics. To summarize, the networks depend on six parameters: the integral scales l_x and l_y; the channel threshold for the accumulated flow c; a and b that transform the hierarchical stream order to channel radii; and the transmissivity of the distributed system T_d. Note that there are no spatial constraints regarding the channel locations, besides moulins that signal the channels' starting points. If a channel location is known (e.g., outlet position), further conditioning could be achieved by extending the gradual deformation method at the cost of extra parameters [*Hu*, 2000]. Figure 3 presents several examples of channel networks plotted on top of ϕ_R. The channel networks were generated using basal and moulin recharge for a synthetic ice sheet. Figures 3a-b have isotropic ϕ_R with different integral scales. Figures 3c-d have anisotropic ϕ_R and Figures 3e-f show the influence of parameter c for the densification of the channels. In the figures, the channel width (blue lines) is proportional to the radius. Note that moulins may become disconnected if parameter c is set to a very low value (e.g.: Figure 3e).

2.2 Subglacial drainage systems water flow model.

The subglacial drainage system water flow model computes water pressure and tracer-transit times in the domain for a channel network realization. The model is framed in a two-dimensional domain where water movement in the subglacial drainage systems is controlled by the gradient of the hydraulic potential ϕ. In equation 1, p_w is unknown and thus determined in the inversion. Water flow is computed under steady-state conditions for a fixed channel geometry and distributed system. Note that we do not consider transient melt-opening and creep-closure of the channels [e.g.:*Werder et al.*, 2013].

The distributed system is modeled as a two-dimensional equivalent-porous-medium layer, and is discretized in uniformly sized quadrangle elements. Water mass conservation assuming incompressibility and pressurized flow is given by the volume conservation equation

$$\nabla \cdot q = m, \qquad (6)$$

with q corresponding to the flux, and m to a prescribed source term. Laminar flow is considered under the assumptions of a non-deformable porous medium:

$$q = -T_d \nabla \phi, \qquad (7)$$

with T_d the transmissivity of the distributed system, and $\nabla\phi$ the gradient of the hydraulic potential. Inserting Eq.(7) into Eq.(6) results in a linear, elliptic equation for ϕ. Note that other studies have modeled flow in the linked cavity system using the Darcy-Weisbach law, which represents turbulent flow [*Flowers*, 2015; *Werder et al.*, 2013].

The channel network is modeled using one-dimensional cylindrical elements of radius r, which are coupled to the distributed system. As mentioned above, we assume that under steady-state flow, the channel opening and closing terms balance and, therefore, are not considered. Similarly, water mass conservation assuming incompressibility and pressurized flow is given by

$$\nabla \cdot Q = m, \qquad (8)$$

with Q the water flow and the derivative taken along the channel axis. In equation (8), the time derivative term of the channel cross-sectional area is not included as it is zero due to pressurized flow and a temporally fixed channel cross-sectional area (Eq.(5)). The discharge Q is computed using the non-linear Manning-Strickler law for turbulent flow

$$Q = -K\nabla\phi, \tag{9}$$

with

$$K = \frac{\alpha\left({}^{r}/_{2}\right)^{2/3}}{n_m\sqrt{|\nabla\phi|}}, \tag{10}$$

where K corresponds to the channel hydraulic conductivity, with a circular cross-section $\alpha=\pi r^2$, n_m is the Manning friction coefficient [*Cornaton*, 2007]. Inserting equations (10) and (9) into (8) leads to a non-linear, elliptic equation for ϕ.

Both components of subglacial drainage systems (channels and distributed systems) are coupled by using a finite-element mesh with shared nodes, assuming continuity of the pressure field [*Cornaton*, 2007]. This allows water and mass exchanges between the distributed system and channels and vice-versa driven by the pressure gradient. This type of coupling has been used in previous subglacial models, for example *Schoof* [2010], *Hewitt* [2011] and *Werder et al.* [2013]. Following such previous work, our model is set up with prescribed water recharge and boundary conditions, such that the bedrock is considered impermeable and the discharge at the outlet is modeled as a fixed pressure (Dirichlet) boundary condition set to atmospheric pressure. Along the rest of the boundary we impose no-flow (Neumann) conditions. The flow equations are solved using the finite element code GROUNDWATER [*Cornaton*, 2007].

As transient mass transport is computationally expensive, we compute transit time using a particle-tracking method based on the advective velocity field obtained from the water pressure field. From an injection point (e.g., moulin), the advective velocity along the particle path is integrated to obtain the transit time. If a particle reaches a channel, it then follows the channel until the outlet.

2.3 Inversion procedure

We use Bayesian inversion to obtain channel networks that are conditioned to observations of water pressure and tracer-breakthrough-curves. Our goal is to determine the combination of model parameter values $\mathbf{m} = [a, b, c, T_d, l_x, l_y]$ describing the network that are able to reproduce the observed data.

The previous sections have described how, starting from a set of model parameters, we can simulate pressure and mass transport in the domain. This is typically referred to as the forward problem, often represented in geophysics and hydrogeology as $\mathbf{d}_{\mathrm{sim}}=g(\mathbf{m})$, where $\mathbf{m}$ is the vector of model parameters, $g(\mathbf{m})$ is the corresponding forward response, and $\mathbf{d}_{\mathrm{sim}}$ corresponds to the simulated values (water pressure and tracer-transit times) [*Mosegaard and Tarantola*, 1995]. In the forward setting, the input parameters $\mathbf{m}$ are known and are mapped to a particular set of model outputs $\mathbf{d}_{\mathrm{sim}}$. Solving the inverse problem amounts to finding values for $\mathbf{m}$ such that the outputs $\mathbf{d}_{\mathrm{sim}}$ match the observations $\mathbf{d}_{\mathrm{obs}}$ to within a prescribed margin of error. Given the typical data scarcity and measurement errors, geophysical and hydrogeological inverse problems are often underdetermined, meaning that many different sets of model parameters can explain the data. One general framework to solve such inverse problems is to use a probabilistic inverse approach based on Bayes' theorem [e.g.: *Linde et al.*, 2015; *Mosegaard and Tarantola*, 1995]:

$$p(\boldsymbol{m}|\boldsymbol{d}) \propto p(\boldsymbol{d}|\boldsymbol{m})p(\boldsymbol{m}), \tag{11}$$

where the left-hand term corresponds to the distribution of the model parameters **m** conditioned to the data **d**, or posterior distribution. According to Bayes' theorem, the posterior distribution is proportional to the product of the likelihood $L(\mathbf{m}|\mathbf{d}) \equiv p(\mathbf{d}|\mathbf{m})$, which describes how likely it is that a proposed model gave rise to the observed data, and the prior $p(\mathbf{m})$, which corresponds to the assumed distribution of model parameters before consideration of the data. The log-likelihood is often used, denoted $\ell(\mathbf{m}|\mathbf{d})$. Assuming independent Gaussian observation errors, the log-likelihood function is given by [*Rosas-Carbajal et al.*, 2014]:

$$\ell(\boldsymbol{m}|\boldsymbol{d}) = -\frac{n}{2} log\, 2\pi - \frac{1}{2} log\left(\prod_{i=1}^{n} \sigma_i^2\right) - \frac{1}{2}\sum_{i=1}^{n}\left(\frac{g_i(\boldsymbol{m})-d_i}{\sigma_i}\right)^2 \tag{12}$$

where *n* corresponds to the number of observations and σ_i is the standard deviation of the observation errors. In practice, σ_i incorporates not only measurement errors, but also attempts to account for structural and epistemic errors. The observations in this case correspond to water pressure and tracer-transit times. The error variance for the pressure is considered absolute, that is, σ_i is not dependent on the value of the measurement. However, for tracer-transit times we considered $\sigma_i = \boldsymbol{\epsilon}\, d_i$, where $\boldsymbol{\epsilon}$ is the relative error as it is expected that longer transit times will present larger error variances than shorter transit times.

The posterior distribution is estimated using a Markov-chain-Monte-Carlo (MCMC) approach, which generates samples proportionally to the posterior probability of occurrence. The procedure consists of: 1) Choosing an arbitrary starting point $\mathbf{m}_{\mathrm{old}}$ from the prior distribution; 2) Proposing a new model $\mathbf{m}_{\mathrm{new}}$ by perturbing the current model using a symmetric proposal distribution; 3) Rejecting or accepting the model with probability [*Mosegaard and Tarantola*, 1995]:

$$\mathrm{P}_{accept} = \min\{1, \exp[\ell(\mathbf{m}_{new}|\mathbf{d}) - \ell(\mathbf{m}_{old}|\mathbf{d}))]\}. \tag{13}$$

If the new model is accepted, then set $\mathbf{m}_{\mathrm{new}}$=$\mathbf{m}_{\mathrm{old}}$. Otherwise, the Markov chain remains at the current point $\mathbf{m}_{\mathrm{old}}$.

Steps 2-3 are iterated until enough samples are computed to represent the posterior distribution. The posterior distribution is computed based on the last 30% of the chains to leave out the burn-in period. Convergence is assessed by the Gelman-Rubin statistic [*Gelman and Rubin*, 1992], which compares the posterior distribution for all the parameters of different MCMC chains for the same inversion configuration. The smaller the difference between the posterior distributions, the smaller is the Gelman-Rubin statistic. Generally, it is consider that the posterior reaches convergence when the Gelman-Rubin statistic is smaller than 1.2 [*Rosas-Carbajal et al.*, 2014]. One of the challenges of using this approach is to define an appropriate symmetric proposal distribution to move from $\mathbf{m}_{\mathrm{old}}$ to $\mathbf{m}_{\mathrm{new}}$, as it greatly influences the computational performance of the inversion and the number of iterations needed to reach convergence. To this end, we use an adaptive MCMC algorithm: $\mathrm{DREAM}_{(\mathrm{ZS})}$ [*Laloy and Vrugt*, 2012]. This algorithm uses multiple parallel chains and an adaptive proposal distribution based on an archive of past states. This enables fast convergence without compromising ergodicity properties.

3 Model setting and context

To test our model in a controlled setting, we apply it to a synthetic configuration based on SHMIP from *Werder et al.* [2017]. SHMIP provides a series of synthetic subglacial settings with diverse recharge scenarios that enables the comparison of subglacial models. From this, we selected as our reference the outputs generated by the subglacial drainage model GlaDS [*Werder et al.*, 2013]. Note that GlaDS represents channels as emergent features of physical processes, such as channel opening by melt and closing by ice creep, which are not considered in our model. Nevertheless, outputs of GLaDS correspond to steady-state simulations where the difference between the opening and closing terms is small. In addition, GLaDS uses the Darcy-Weisbach law to model the water flow whereas we use the Darcy law in the distributed system and the Manning-Stickler law for the channels. Even though GLaDS is a state-of-the-art process-based model, it does not represent the real complexity of subglacial drainage systems and issues still need to be addressed (e.g.: mesh sensitivity). This is discussed in Section 5. This setting enables us to evaluate whether our methodology allows us to infer a channel structure and hydraulic properties that were generated by a much more complex model involving processes that are not explicitly taken into account in our formulation. Water pressure data and tracer-transit times are extracted from the GlaDS simulations, which constitute the synthetic data set. By using a synthetic case, we are able to explore different recharge conditions, different amounts of data, and quantify uncertainty against a fully known reference, which is currently not available for real glacier systems.

All test cases have identical geometries and boundary conditions: a rectangular domain of 20 km by 100 km with an ice sheet geometry consisting of a flat bedrock and an ice sheet elevation approximated with a parabolic function varying with the distance to the glacier snout. As a result, the ice thickness increases from zero at x=0 to 1521 m at x=100 km. No-flow boundary conditions are imposed on the three inner boundaries and a fixed pressure boundary condition is set to atmospheric pressure at the x=0 boundary. The model is discretized in 2D square finite elements of 500 × 500 m that form the distributed system. Channels are represented by 1D elements along the edges of the square grid elements. Channels are not allowed to cross no-flow boundaries. All models are run in steady-state to compute pressures and tracer-transit times.

Three recharge scenarios are considered herein: A4, A5 and B3 (keeping the names used in SHMIP). Scenario A4 has a relatively low basal recharge of 2.5×10^{-8} m s^{-1} (equivalent to 50 m^3 s^{-1} on the entire domain); A5 has a high recharge of 4.5×10^{-8} m s^{-1} (90 m^3 s^{-1}); B3 has a basal recharge of 7.93×10^{-11} m s^{-1} (0.1586 m^3 s^{-1}) and additionally a punctual recharge at 20 moulins (Figure 4a), totaling 90 m^3 s^{-1} (4.5 m^3 s^{-1} for each moulin). Each scenario has associated water pressure measurements and tracer travel times extracted from GLaDS (Figure 4a and

Table **2**). We also designed scenarios with different amounts of data to test the influence of data availability, which are presented in the supplementary material.

Because of the absence of moulins in scenarios A4 and A5, tracer is injected at the locations denoted by a green circle in Figure 4a. As basal recharge is homogeneous and, as noted previously, we do not attempt to infer the exact location of the channels (but rather the network structure), therefore tracer injection point is moved to the closest channel within a radius of 1 km. With this, we aim not to force and bias the network structure to condition it in some specific location. If no channel passes within this distance, the tracer is injected in the distributed system, which can result in a large delay in the transit times. For case B3, injection is done in the moulins marked with a green circle in Figure 4b.

For the subglacial channel generator, we generate ϕ_R using zero mean and a variance of 0.49 MPa. This value was chosen empirically based on a sensitivity analysis (not shown), that established that this is value is enough to influence the structures of the networks. Note that the hydraulic potential varies from 0 to ~15 MPa in the upper part of the ice sheet. For this case of flat bedrock and idealized ice sheet geometry, a small variance in ϕ_R is enough to influence channel orientation.

For the inversion procedure, the variance of the synthetic data errors for the log-likelihood function (eq. 11) has to be defined. Because field observations have shown that water pressure in nearby boreholes can show dissimilar behavior [*Hubbard et al.*, 1995; *Schoof et al.*, 2014]. Also, we need to account for the differences in the physics assumed in this model and in the reference model from GLADs. These suggest that a large variance in water pressure should be considered. For this, we choose a value of 0.5 MPa. Similarly, for the tracer-transit times we consider a relative error equivalent to the 20% of the observed tracer-transit time.

The prior distributions of the model parameters are uniform and log-uniform within bounds, as summarized in Table 3.

4 Results: Inversion of subglacial drainage systems

In this section, we first provide the results of the inversion for each water recharge scenario (A4, A5 and B3), to finish with a section that compares these cases. The value of data varying number of observational settings is presented in the supplementary material.

For each case, a total of 200,000 iterations were run. This number was chosen according to our computational budget. We consider the posterior distribution based on the last 30% of the chain, ensuring that the convergence criteria of the Gelman-Rubin statistic <1.2 has been met and that enough independent posterior samples have been considered.

4.1 Distributed low recharge case (A4)

The inversion results for this case show a marked reduction in the uncertainty of model parameters a, and T_d, as shown in the marginal probability density function (pdf) or the posterior histogram of these parameters (the diagonal elements of Figure 5). For example, parameter T_d, shows a narrow distribution around $10^{-0.93}$ m^2 s^{-1}. Note that the prior ranges from 10^{-4} to $10^{-0.5}$ m^2 s^{-1} and in Figure 5 the x-axis ranges from 10^{-2} to $10^{-0.5}$ m^2 s^{-1}. The joint probability distributions of each pair of variables are shown as density plots below the diagonal. It is important to note that the prior distributions are uniform or log-uniform (Table 3). Therefore, a reduction in uncertainty occurs when the posterior pdf takes on preferred values within these ranges. Case A4 has a distributed recharge; therefore, the narrow distribution of T_d confirms the importance of the distributed system when most of the recharge is homogenously distributed. Another parameter that shows significant uncertainty reduction is a (the linear scaling of the channels' radii), suggesting a value close to zero, which implies very small channels. Parameters l_x and l_y, are not well constrained and exhibit multiple modes, none dominant.

To illustrate the spatial characteristics of the channel networks, we present a selection of models: three models randomly chosen from the posterior distribution (r1, r2 and r3), the maximum likelihood model (mx), the mean effective pressure of all posterior models (x), and the reference from SHMIP A4. The models are presented in Figure 6a. Models r1, r2 and r3 show a tendency to have one dominant channel concentrating most discharge. Model mx shows one dominant channel with a secondary parallel channel having common characteristic to the reference model. Nevertheless, it is important to keep in mind that these are only samples of posterior models. In the effective pressure profile for the selected models (Figure 6b), it can be seen that even though there is a generally good match with the reference, the main mismatch occurs at the same location for most the models, around 10 km away from the outlet. Lastly, Figure 6c presents the distribution of the transit times for the two tracer tests. The transit time distribution is narrower for the injection point that is closer to the outlet (Figure 4).

4.2 Distributed high recharge case (A5).

Posterior inversion results for recharge case A5 show a significant uncertainty reduction of parameters a, b and T_d compared to the prior (see Figure 7). In addition, parameter c shows a threshold at 10^{-2}, which corresponds to the minimum required for channelization. Moreover, parameters l_x and l_y show little uncertainty reduction from their prior distribution. One explanation is that the amount of data does not allow distinguishing between different channel structures. Several correlations are visible in the joint density plots. Parameters a and b are inversely related and T_d shows significant dependences, especially with a and b. Indeed, it is expected that T_d influences other parameters as it controls the redistribution of water fluxes in the glacier.

Posterior model samples for case A5 show the common characteristic of two roughly parallel channels (Figure 8a). The channels are mostly straight and show no major branching, as in the A5 reference model. From the effective pressure profile (Figure 8b), it seems that the pressure is well constrained around the reference model (black line). Again, there is an important mismatch in the first 10 km. Note that model r3 is able to reproduce the 10 km effective pressure peak

4.3 Moulins and distributed recharge case (B3)

Case B3 is a particularly interesting example because it has input from moulins. Parameters a, b and T_d are well constrained although the distribution includes one or multiple modes (Figure 9). Parameter c shows a uniform distribution between $10^{-1.3}$ and the lower bound, meaning that there is a minimum necessary connectivity or channel densification to fit the data ($10^{-1.3}$ percent of the total water recharge is approximately 4.5 m^3 s^{-1}, the recharge on the moulin). Parameter T_d, shows one mode, but not as pronounced as in case A5. Since most of the water recharge occurs via moulins, channel-related parameters are more influential. Another notable feature is that parameters l_x and l_y present multiple modes. This is consistent with other channel-dependent parameters, as in this case most of the flow is channelized. Consequently, the information provided in this case enables inferring spatial properties of the network structure.

Similar to previous cases, a selection of posterior models is presented to explore the results for this case (Figure 10). One distinct feature observed is that the discharge in some channels decreases downstream (Figure 10a, case r3 and mx). This is also observed in the reference model (Figure 10a, reference case B3). A cross section of the effective pressure is presented in Figure 10b, where it can be seen that the pressure is constrained and most of the models are between 0.5 MPa apart from the reference. The first 10 km of the effective pressure present an important mismatch. Figure 10c presents the histogram of the transit times for three tracer-tests carried out in moulins. The mode of the histogram for the first two tracer tests show good agreement with the reference value. However, the third tracer-test shows an important mismatch of 10 hours (3 hours for the mx model).

4.4 Comparison of recharge scenarios

To highlight the differences in the subglacial systems under different recharge conditions, the posterior distribution of the model parameters for the three recharge scenarios is shown in Figure 11a. The first parameter a represents a linear scaling of the network, b the relative size between the different stream order of the channel network, and c the threshold where channels are modelled explicitly. The T_d correspond to the transmissivity of the distributed system and to explore the global changes in the channel network, we introduce an aggregated variable: the total channelized volume (t_{cv}) which depends on the parameters a, b, c, l_x and l_y. The channelized total volume is computed as the sum of the channels length, times the cross section of each channel segment.

A first remark is the gradual increase in a from A4 (low water recharge) to A5 (high water recharge), then from A5 to B3 (similar recharge). For the distributed system T_d increases from A4 to A5, however for case B3 it is relatively lower. The channel network plays an import role in case B3 because of the presence of moulins. This explains the high value for a and the low value for T_d. Parameter b, which represents the range of radii within the channel network, takes a lower value for case B3, meaning similar radii for the upper and lower parts of the network. In case A5, b is centered on 2.5, meaning that matching the data requires larger channels downstream in the network. Case A4 presents multiple modes, which is not surprising since the channels are relatively small in radius (parameter a). Moreover, the distributed system (controlled by T_d) being dominant in this system, parameter b does not play an important role in this case. Additionally, the mode of t_{cv} is low for A4 and higher for A5 and B3. This confirms that in A4, the channel network has a relatively smaller volume.

The relation between the distributed and channelized system for the different recharge cases is best represented by a scatter plot of T_d vs t_{cv} (Figure 11b) Case B3 is dominated by channels, therefore variations in T_d do not affect the overall behavior, represented by t_{cv}. This is not the case for A4 and A5, where a small variation in T_d has a large effect on t_{cv}, suggesting a dominance of the distributed system. However, for case A5, there is a bigger constrain on t_{cv}, meaning that the channelized system is still relevant.

In summary, the higher recharge scenarios B3 and A5 result in larger values for parameter a. This is accompanied by an increase of T_d by one order of magnitude. It can be seen that the t_{cv} increases for case A3 to A5 and B3, whereas for case B3 it is much more constrained. This can be explained by the presence of moulins (case B3) that result in the distributed system being less influential.

5 Discussion

5.1 Model validation

Results show that the developed framework in this study is able to capture main features of the reference model. The effective pressure field of the synthetic ice-sheet is generally well represented, with the notable exception of the first 10 km as discussed below. The middle and upper sections of the ice-sheet present low hydraulic gradients and water flow is dominated by the distributed system. Basal recharge strongly influences the transmissivity of the distributed system (T_d). This is captured in the Bayesian inference by a constrained posterior distribution for this parameter. One reason for the pressure misfit in the lower section of the ice sheet is the different representation of the flow in our model and in GLaDS. We chose the radius equation (eq. 5) and a homogeneous transmissivity, whereas the approach used in GLaDS considers an opening-closure channel relationship determining the radius and varying water sheet thickness. Close to the terminus, hydraulic gradients are larger and a laminar model in the distributed system is not favored by this behavior. Case B3 that includes moulins shows a stronger dominance of the channelized system compared to cases A4 and A5. This can be seen in the posterior distribution of parameter *a*, which scales the radii sizes, as well as in the total channelized volume (t_{cv}).

Another reason for this mismatch is the location of the pressure measurements. In the 21-borehole spatial array, none of the boreholes is close to the effective pressure peak at 10 km. Different spatial arrays are presented in the supplementary material, showing a better match in cases where boreholes are located in the first few kilometers from the outlet. Note that we are able to observe this misfit because we have access to the exhaustive synthetic outputs from GLaDS. In the supplementary material, we show an analysis of the uncertainty reduction by considering 1, 3, 8 and 21 boreholes, with and without tracer-test measurements.

5.2 Forward model: Limitations and further work

The core idea of our channel generator is the incorporation of a perturbation term ϕ_R in the hydraulic potential. The impact of ϕ_R will depend on the shape of the hydraulic potential field. In this study, the synthetic flat bedrock and idealized ice sheet result in a smooth hydraulic potential field, and consequently ϕ_R is a determining factor for the channel-network structure. However, in cases where ice sheets or glacier valleys lie on top of known complex topography, ϕ_R will play a less important role by influencing, for example, only the channel sinuosity within limits imposed by the bedrock topography. Another assumption of our channel generator is that of $N = 0$ (eq. 3). Other models use the assumption of $p_w = f\, p_i$ where f is spatially uniform a flotation factor usually varying between 0.6 to 1.1 [*Chu et al.*, 2016]. This assumption is insignificant for a flat-bed setting, but for complex topographies it has been shown that variations in f can be significant [*Chu et al.,* 2016]. While the variance of ϕ_R and f are prescribed in this paper, for applications with more complex topographies it is possible to include the ϕ_R variance and f as additional parameters in the inversion. Another modeling choice we make is that the structural Gaussian deformation is carried out by modifying l_x and l_y in directions parallel and perpendicular to the ice flow. This allows producing a variety of channel networks, from arborescent to long parallel channels. Nevertheless, this could be revisited in case of complex topography, considering for example cases of asymmetry or curved flow lines in glaciers and ice sheets.

In the A4 and A5 scenarios, the channel locations are poorly constrained. This is not the case for B3 where the presence of moulins determines the channel locations. By fixing the white noise (or random seed) of ϕ_R in case A3, we reduce the number of degrees of freedom, enabling us to infer the network structure, but not the exact location of channels.

A further improvement could be to consider the outlet location or any known channel segments. For ground-terminating glaciers, the outlet location is often known and channels-end could be pinned to the known location. This could be incorporated as an acceptance/rejection rule in the prior networks (before running the water flow model), where only the channel networks matching the known locations are considered for the next step. Additionally, the proportion of water discharge at each outlet could be used as information as well. For this study, we focused on the overall network geometry, but further studies should include known channel sections. If a large amount of such local data are to be considered, the approach of Gaussian gradual deformation [*Hu*, 2000] could be considered, along with the additional parameterization it involves.

An assumption of our model is the continuity of channels along the hydraulic potential. This excludes the possibility of channels splitting downwards the hydraulic potential. This is the results of levelling the local depressions in the perturbed hydraulic potential, inherent to the D8 routing algorithm [*O'Callaghan and Mark*, 1984]. Several studies [e.g.: *Chu et al.*, 2016] propose to use D∞ routing algorithm [*Tarboton*, 1997] to account for the divergence of flow paths. Additionally, not levelling the local depressions in the perturbed hydraulic potential map could be used to stop channels in areas of flat or negative gradient. The incorporation of these features would require extra parameters, but is possible and could be explored in further research. Note that our results for case B3 show that channels can already be present on pressure ridges where water leaks to the distributed system, as also found in *Werder et al.* [2013].

Regarding the flow model, Darcy's laminar flow was considered in the distributed system. Results for case A5 inferred the highest values for the transmissivity to be on the order of $10^{-0.6}$ $m^2 s^{-1}$; a value at which the laminar flow assumption should be considered with caution. Therefore, in our study some of the obtained values of T_d may not correspond to physical parameters, but instead might correspond to surrogate parameters.

5.3 Inversion framework

The likelihood function was defined assuming: (i) uncorrelated independent Gaussian errors; and (ii) known variances of the observations (water pressure and tracer-transit times) and known model errors. Here, we arbitrarily assigned the error variance (model errors and observation errors considered together) which enables us to compare the different posteriors in relative terms. However, increasing or decreasing the error variance will lead to a wider or narrower posterior distribution. Quite importantly, further work should also explore retrieving the uncertainty from model errors as well as a general likelihood function considering non-Gaussian errors and correlation of errors in non-linear problems [*Schoups and Vrugt*, 2010]

We emphasize that parsimony is an important requirement for geostatistical approaches involving inversion. It is a price to pay for models capable of data conditioning and uncertainty quantification. More realistic models for the networks could include heterogeneous channel friction coefficients and more complex network parameterization, but this would in turn imply having additional parameters, which would be difficult to estimate using a Bayesian inversion framework. Note that the posterior models are not a description of the subglacial system itself, but a set of surrogate parameters that characterize geostatistical properties of the subglacial drainage system. For example, we model a homogeneous distributed system with transmissivity T_d, but there are an infinite number of heterogeneous transmissivity fields that could fit the data equally well. We could add more complexity to the channel generator, but without observations it would result in the parameters becoming more undetermined.

6 Conclusions

In this study, we propose a framework to generate an ensemble of channel networks that honor water-pressure and tracer-transit-time data. The subglacial channel network connectivity and spatial structure are inferred through an inversion of pressure and tracer-transit times. An important benefit is that it enables uncertainty quantification of the model parameters, at the cost of limited physical insights and no time evolution of the system. One of the novelties of this framework is that the subglacial channels are generated through a combination of geostatistical and physical processes. This contrasts to purely physical-process-based models [e.g.: *Schoof*, 2010; *Werder et al.*, 2013], where channels are an emerging property of physical or empirical laws, but which are difficult to condition to data. Our framework can be seen as complementary, because it proposes channel networks constrained by observations rather than a result of a process-based model.

Three recharge scenarios were tested, representing the state of subglacial drainage systems at different periods of the year. It was found that each recharge scenario has distinctive model parameters, where a low water recharge produces smaller channels and less total channelized volume, associated with lower values of transmissivity for the distributed system, suggesting that the approach could be used to capture snapshots of subglacial systems across a season. As including temporal variations of the system could be computationally challenging, insights in the evolution of the system can be gained by comparing the system at different instantaneous states and recharge conditions.

Further work should consider a real case scenario as well as incorporating other data sources, such as the location of multiple outlets and their relative discharge or seismic tremor data [e.g.: *Gimbert et al.*, 2016]. This study was limited in assessing the uncertainty of the model parameters, but the uncertainties from water recharge, boundary conditions, bedrock topography and other variables of interest could be addressed as well. It also remains to be tested if the posterior model realizations can be used to make predictions. For example, one could consider the effective pressure maps to explore the variability on basal sliding when coupled with an ice flow model or test the channel networks response to outburst floods or sediment transport capacity.

Acknowledgments

We thank Fabien Cornaton (DHI WASY GmbH) for his support regarding the use of the GROUNDWATER code. I.I. acknowledges support from CONICYT through Becas Chile program. Lastly, we would like to thank to the anonymous reviewers for their comments and suggestions. No new data were used in producing this manuscript. Model results can be downloaded from https://zenodo.org/deposit/2593785.

7 References

Arnold, N., K. Richards, I. Willis, and M. Sharp (1998), Initial results from a distributed, physically based model of glacier hydrology, Hydrological Processes, 12(2), 191-219, doi: 10.1002/(SICI)1099-1085(199802)12:2<191::AID-HYP571>3.0.CO;2-C.

Benn, D. I., and D. J. A. Evans (2010), Glaciers and Glaciation., 802 pp., Hodder Education, London.

Borghi, A., P. Renard, and S. Jenni (2012), A pseudo-genetic stochastic model to generate karstic networks, Journal of Hydrology, 414-415, 516-529, doi: 10.1016/j.jhydrol.2011.11.032.

Borghi, A., P. Renard, and F. Cornaton (2016), Can one identify karst conduit networks geometry and properties from hydraulic and tracer test data?, Advances in Water Resources, 90, 99-115, doi: 10.1016/j.advwatres.2016.02.009.

Brinkerhoff, D. J., C. R. Meyer, E. Bueler, M. Truffer, and T. C. Bartholomaus (2016), Inversion of a glacier hydrology model, Annals of Glaciology, FirstView, 1-12, doi: doi:10.1017/aog.2016.3.

Chandler, D. M., et al. (2013), Evolution of the subglacial drainage system beneath the Greenland Ice Sheet revealed by tracers, Nature Geoscience, 6(3), 195-198, doi: 10.1038/ngeo1737.

Chu, W., T. T. Creyts, and R. E. Bell (2016), Rerouting of subglacial water flow between neighboring glaciers in West Greenland, Journal of Geophysical Research: Earth Surface, 121(5), 925-938, doi: 10.1002/2015JF003705.

Cornaton, F. (2007), Ground water : A 3-d ground water and surface water flow, mass transport and heat transfer finite element simulator, Internal Report thesis, University of Neuchuatel, Neuchuatel.

Covington, M. D., A. F. Banwell, J. Gulley, M. O. Saar, I. Willis, and C. M. Wicks (2012), Quantifying the effects of glacier conduit geometry and recharge on proglacial hydrograph form, Journal of Hydrology, 414-415, 59-71, doi: 10.1016/j.jhydrol.2011.10.027.

Cuffey, K. M., and W. S. B. Paterson (2010), The physics of glaciers, 4th ed. ed., xii, 693 p. pp., Butterworth-Heinemann/Elsevier, Burlington, Mass.

De Fleurian, B., et al. (2018), SHMIP The subglacial hydrology model intercomparison Project, 1-20 pp.

Flowers, G. E. (2015), Modelling water flow under glaciers and ice sheets, Proceedings of the Royal Society A: Mathematical, Physical and Engineering Sciences, 471(2176), 20140907-20140907, doi: 10.1098/rspa.2014.0907.

Fountain, A. G., and J. S. Walder (1998), Water flow through temperate glaciers, Reviews of Geophysics, 36(3), 299-328, doi: 10.1029/97rg03579.

Gelman, A., and D. B. Rubin (1992), Inference from Iterative Simulation Using Multiple Sequences, Statist. Sci., 7(4), 457-472, doi: 10.1214/ss/1177011136.

Gimbert, F., V. C. Tsai, J. M. Amundson, T. C. Bartholomaus, and J. I. Walter (2016), Subseasonal changes observed in subglacial channel pressure, size, and sediment transport, Geophysical Research Letters, 43(8), 2016GL068337, doi: 10.1002/2016GL068337.

Gulley, J. D., M. Grabiec, J. B. Martin, J. Jania, G. Catania, and P. Glowacki (2012), The effect of discrete recharge by moulins and heterogeneity in flow-path efficiency at glacier beds on subglacial hydrology, Journal of Glaciology, 58(211), 926-940, doi: 10.3189/2012JoG11J189.

Gulley, J. D., P. D. Spellman, M. D. Covington, J. B. Martin, D. I. Benn, and G. Catania (2014), Large values of hydraulic roughness in subglacial conduits during conduit enlargement: implications for modeling conduit evolution, Earth Surface Processes and Landforms, 39(3), 296-310, doi: 10.1002/esp.3447.

Herman, F., F. Beaud, J.-D. Champagnac, J.-M. Lemieux, and P. Sternai (2011), Glacial hydrology and erosion patterns: A mechanism for carving glacial valleys, Earth and Planetary Science Letters, 310(3-4), 498-508, doi: 10.1016/j.epsl.2011.08.022.
Hewitt, I. J. (2011), Modelling distributed and channelized subglacial drainage: the spacing of channels, Journal of Glaciology, 57(202), 302-314, doi: 10.3189/002214311796405951.
Hu, L. Y. (2000), Gradual Deformation and Iterative Calibration of Gaussian-Related Stochastic Models, Mathematical Geology, 32(1), 87-108, doi: 10.1023/a:1007506918588.
Hu, L. Y., and M. Le Ravalec-Dupin (2004), Elements for an Integrated Geostatistical Modeling of Heterogeneous Reservoirs, Oil & Gas Science and Technology - Rev. IFP, 59(2), 141-155.
Hubbard, B. P., M. J. Sharp, I. C. Willis, M. K. Nielsen, and C. C. Smart (1995), Borehole water-level variations and the structure of the subglacial hydrological system of Haut Glacier d'Arolla, Valais, Switzerland, Journal of Glaciology, 41(139), 572-583.
Huss, M., A. Bauder, M. Werder, M. Funk, and R. Hock (2007), Glacier-dammed lake outburst events of Gornersee, Switzerland, Journal of Glaciology, 53(181), 189-200, doi: 10.3189/172756507782202784.
Iken, A. (1981), The Effect of the Subglacial Water Pressure on the Sliding Velocity of a Glacier in an Idealized Numerical Model, Journal of Glaciology, 27(97), 407-421, doi: 10.3198/1981JoG27-97-407-421.
Kamb, B. (1987), Glacier surge mechanism based on linked cavity configuration of the basal water conduit system, Journal of Geophysical Research: Solid Earth, 92(B9), 9083-9100, doi: 10.1029/JB092iB09p09083.
Koppes, M., B. Hallet, E. Rignot, J. Mouginot, J. S. Wellner, and K. Boldt (2015), Observed latitudinal variations in erosion as a function of glacier dynamics, Nature, 526(7571), 100-103, doi: 10.1038/nature15385.
Laloy, E., and J. A. Vrugt (2012), High-dimensional posterior exploration of hydrologic models using multiple-try DREAM(ZS) and high-performance computing, Water Resources Research, 48(1), doi: doi:10.1029/2011WR010608.
Le Ravalec, M., B. Noetinger, and L. Y. Hu (2000), The FFT Moving Average (FFT-MA) Generator: An Efficient Numerical Method for Generating and Conditioning Gaussian Simulations, Mathematical Geology, 32(6), 701-723, doi: 10.1023/a:1007542406333.
Linde, N., P. Renard, T. Mukerji, and J. Caers (2015), Geological realism in hydrogeological and geophysical inverse modeling: A review, Advances in Water Resources, 86, 86-101, doi: 10.1016/j.advwatres.2015.09.019.
Linde, N., D. Ginsbourger, J. Irving, F. Nobile, and A. Doucet (2017), On uncertainty quantification in hydrogeology and hydrogeophysics, Advances in Water Resources, 110, 166-181, doi: https://doi.org/10.1016/j.advwatres.2017.10.014.
Livingstone, S. J., R. D. Storrar, J. K. Hillier, C. R. Stokes, C. D. Clark, and L. Tarasov (2015), An ice-sheet scale comparison of eskers with modelled subglacial drainage routes, Geomorphology, 246, 104-112, doi: 10.1016/j.geomorph.2015.06.016.
Mariethoz, G., P. Renard, and J. Caers (2010), Bayesian inverse problem and optimization with iterative spatial resampling, Water Resources Research, 46(11), n/a-n/a, doi: 10.1029/2010wr009274.

Mosegaard, K., and A. Tarantola (1995), Monte Carlo sampling of solutions to inverse problems, Journal of Geophysical Research: Solid Earth, 100(B7), 12431-12447, doi: 10.1029/94JB03097.

Nienow, P. W., M. Sharp, and I. C. Willis (1996), Velocity-discharge relationships derived from dye tracer experiments in glacial meltwaters: Implications for subglacial flow conditions, Hydrological Processes, 10(10), 1411-1426, doi: https://doi.org/10.1002/(SICI)1099-1085(199610)10:10<1411::AID-HYP470>3.0.CO;2-S

Nye, J. F. (1976), Water flow in glaciers: jökulhlaups, tunnels and veins, Journal of Glaciology, 17, 181-207.

O'Callaghan, J. F., and D. M. Mark (1984), The extraction of drainage networks from digital elevation data, Computer Vision, Graphics, and Image Processing, 28(3), 323-344, doi: http://dx.doi.org/10.1016/S0734-189X(84)80011-0.

Rongier, G., P. Collon-Drouaillet, and M. Filipponi (2014), Simulation of 3D karst conduits with an object-distance based method integrating geological knowledge, Geomorphology, 217, 152-164, doi: http://dx.doi.org/10.1016/j.geomorph.2014.04.024.

Rosas-Carbajal, M., N. Linde, T. Kalscheuer, and J. A. Vrugt (2014), Two-dimensional probabilistic inversion of plane-wave electromagnetic data: methodology, model constraints and joint inversion with electrical resistivity data, Geophysical Journal International, 196(3), 1508-1524, doi: 10.1093/gji/ggt482.

Röthlisberger, H. (1972), Water pressure in intra and subglacial channels, Journal of Glaciology, 11(62), 177-203.

Schoof, C. (2010), Ice-sheet acceleration driven by melt supply variability, Nature, 468(7325), 803-806, doi: 10.1038/nature09618.

Schoof, C., C. A. Rada, N. J. Wilson, G. E. Flowers, and M. Haseloff (2014), Oscillatory subglacial drainage in the absence of surface melt, The Cryosphere, 8(3), 959-976, doi: 10.5194/tc-8-959-2014.

Schoups, G., and J. A. Vrugt (2010), A formal likelihood function for parameter and predictive inference of hydrologic models with correlated, heteroscedastic, and non-Gaussian errors, Water Resources Research, 46(10), doi: doi:10.1029/2009WR008933.

Schuler, T., U. H. Fischer, and G. H. Gudmundsson (2004), Diurnal variability of subglacial drainage conditions as revealed by tracer experiments, Journal of Geophysical Research: Earth Surface, 109(F2), n/a-n/a, doi: 10.1029/2003JF000082.

Schwanghart, W., and D. Scherler (2014), Short Communication: TopoToolbox 2 – MATLAB-based software for topographic analysis and modeling in Earth surface sciences, Earth Surf. Dynam., 2(1), 1-7, doi: 10.5194/esurf-2-1-2014.

Shreve (1966), Statistical law of stream numbers, The Journal of Geology, 17-37.

Shreve (1972), Movement of water in glaciers, Journal of Glaciology, 11, 205-214.

Tarboton, D. G. (1997), A new method for the determination of flow directions and upslope areas in grid digital elevation models, Water Resources Research, 33(2), 309-319, doi: doi:10.1029/96WR03137.

Verbunt, M., J. Gurtz, K. Jasper, H. Lang, P. Warmerdam, and M. Zappa (2003), The hydrological role of snow and glaciers in alpine river basins and their distributed modeling, Journal of Hydrology, 282(1-4), 36-55, doi: 10.1016/s0022-1694(03)00251-8.

Vuilleumier, C., A. Borghi, P. Renard, D. Ottowitz, A. Schiller, R. Supper, and F. Cornaton (2012), A method for the stochastic modeling of karstic systems accounting for geophysical data: an example of application in the region of Tulum, Yucatan Peninsula (Mexico), Hydrogeology Journal, 21(3), 529-544, doi: 10.1007/s10040-012-0944-1.

Walder, J. S. (1986), Hydraulics of Subglacial Cavities, Journal of Glaciology, 32(112), 439-445, doi: 10.3189/S0022143000012156.

Weertman, J. (1972), General theory of water flow at the base of a glacier or ice sheet, Reviews of Geophysics, 10(1), 287-333, doi: 10.1029/RG010i001p00287

Werder, M., I. J. Hewitt, C. G. Schoof, and G. E. Flowers (2013), Modeling channelized and distributed subglacial drainage in two dimensions, Journal of Geophysical Research: Earth Surface, 118(4), 2140-2158, doi: 10.1002/jgrf.20146.

Werder, M., et al. (2017), Subglacial Hydrology Model Intercomparison Project (SHMIP), EGU General Assembly 2017, Vienna, Austria, 24 April 2017 - 28 April 2017., doi: Vol. 19, EGU2017-12783-3, 2017.

Willis, I. C., C. D. Fitzsimmons, K. Melvold, L. M. Andreassen, and R. H. Giesen (2012), Structure, morphology and water flux of a subglacial drainage system, Midtdalsbreen, Norway, Hydrological Processes, 26(25), 3810-3829, doi: 10.1002/hyp.8431.

8 Tables and figures

Table 1. Constants, variables and units.

Parameter	Definition	Value	Units
Model constants			
ρ_w	Water density	1000	kg m^{-3}
ρ_i	Ice density	917	kg m^{-3}
g	Gravitational acceleration	9.81	m s^{-2}
n_m	Manning roughness coefficient	0.04	m$^{-1/3}$ s
f	Flotation factor	1	
Synthetic geometry by SHMIP			
B	Bedrock elevation		m
H	Ice thickness		m
Derived from geometry and constants			
ϕ_z	Elevation potential		MPa
p_i	Ice overburden pressure		MPa
ϕ_s	Shreve's hydraulic potential		MPa
Water flow model variables			
ϕ	Hydraulic potential		MPa
p_w	Water pressure		MPa
q	Sheet discharge		m^2 s^{-1}
Q	Channel discharge		m^{3}s^{-1}
N	Effective pressure		MPa
Variables determined by inversion procedure			
r	Channel radius		m
T_d	Transmissivity distributed system [a]		m^2 s^{-1}
ϕ_R	Gaussian random perturbation (channel network topology)		MPa
Channel generator variables			
a	Radius scaling factor		
b	Radius hierarchical order factor		
c	Flow accumulation channel threshold		% of recharge
l_x	Integral scale east direction		km
l_y	Integral scale north direction		km

[a]Correspond to a variable of the channel network generator as well.

Table 2. Summary of the test cases.

Case	Basal recharge (m s^{-1})	Moulin recharge	Water pressure data (boreholes)	Tracer injection	Distance from outlet (km)	Observed transit time (h)
A4	2.5x10^{-8}	-	21	2 from boreholes	17.5 and 49	17 and 51
A5	4.5x10^{-8}	-	21	2 from boreholes	17.5 and 49	7 and 19
B3	7.93x10^{-11}	20 moulins, 4.5 $m^3 s^{-1}$ each	21	3 from moulins	19, 33 and 47	2.8, 5 and 18

Table 3. Channel generator variables

Parameter	Description	Units	Prior
l_x	Integral scale east direction	km	$U_{[1.5 – 6.5]}$
l_y	Integral scale north direction	km	$U_{[1.5-6.5]}$
a	Radius scaling factor		$U_{[0.1-5]}$
b	Radius hierarchical order factor		$U_{[0.1-5]}$
c	Flow accumulation channel threshold	% of total recharge	$10^{U[-3.6 - -0.6]}$
T_d	Transmissivity of the distributed system	m^2 s^{-1}	$10^{U[-4 - -0.5]}$

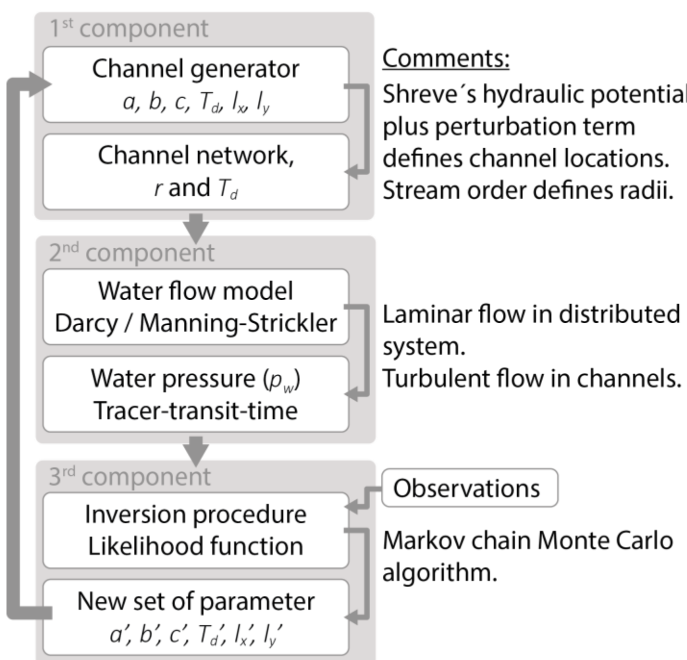

Figure 1: Workflow diagram. The first component produces a two-dimensional channel network. Variables *a*, *b* and *c* define channel radii (*r*), l_x and l_y controls channel locations, and T_d the transmissivity of the distributed system. Then, the second component computes the water flow and tracer-transit times in the previously generated channel network. Finally, the third component compares outputted water pressure and tracer-transit times with data, and proposes a new set of parameters following a probabilistic framework

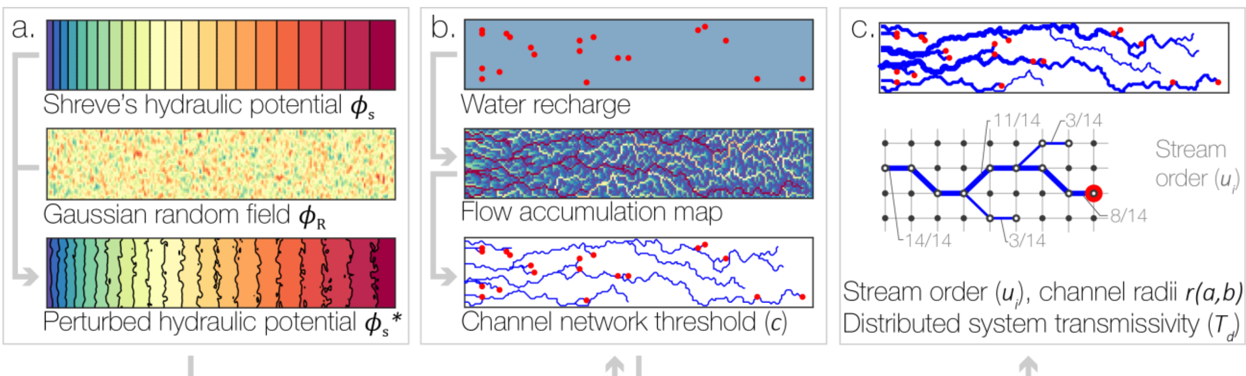

Figure 2. Subglacial channel network generator. (a) The Shreve's hydraulic potential (color scale from 0 – 15 MPa) is computed and a Gaussian random field ϕ_R (color scale from -0.2 to 0.2 MPa) with integral scales l_x and l_y is added to generate the perturbed hydraulic potential (color scale from 0 – 15 MPa). (b) Distributed and punctual (red dots) water recharge, together with the flow routing D8 algorithm on the perturbed hydraulic potential are used to generate the flow accumulation map. Then, a threshold *c* is applied to the flow accumulation to obtain the channel network. (c) From the channel network, the stream order (gray numbers) is used to compute the radius of each channel segment. Note that the threshold *c* is set to 3 and the moulin input is set to 8. Distributed system mesh nodes (black) and common nodes between channels and distributed system (white) are displayed.

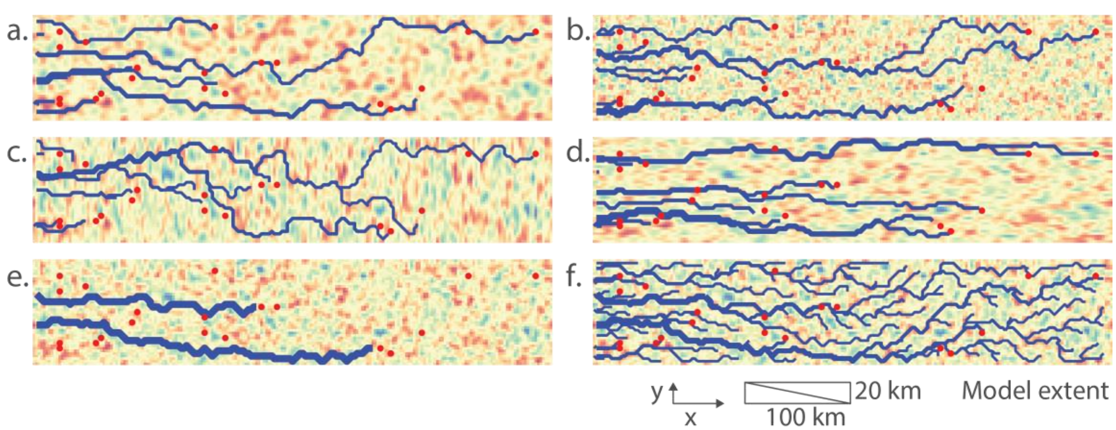

Figure 3. Illustration of different channel networks (blue lines) plotted on top of different ϕ_R for a synthetic ice sheet of 100 × 20 km. The general flow direction is from right to left, and basal and punctual moulin recharge (red dots) are considered. Integral scales l_x and l_y are increasing from (a) to (b). In (c) and (d), we show the effect of anisotropy obtained by introduced by

selecting $l_x > l_y$ and $l_x < l_y$ respectively. In (e) and (f), we show the influence of the threshold c on the densification of the channel network.

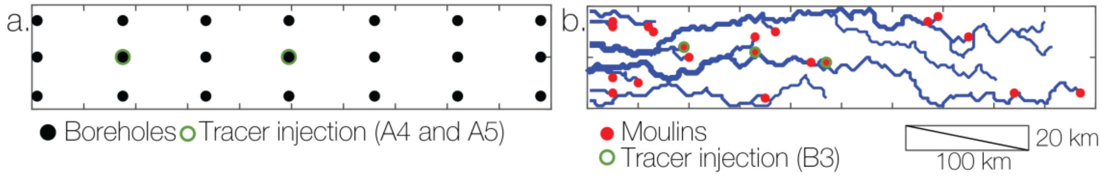

Figure 4. Modeled domain, position of boreholes and moulins. (a) Boreholes location for pressure data (cases A4, A5 and B3) and tracer injection (cases A4 and A5). (b) Moulins and tracer injection locations for case B3 (channels correspond to one realization, for illustration).

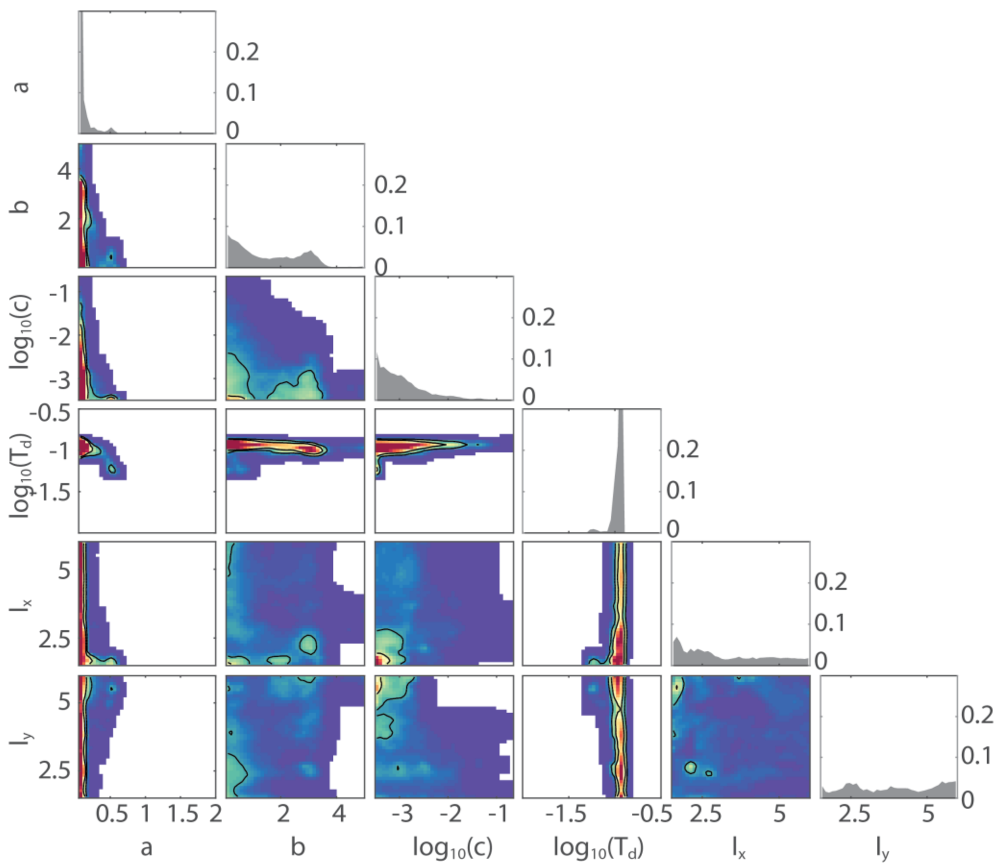

Figure 5. Posterior distributions of the model parameters for case A4_BH21_T2. The diagonal shows the marginal posterior pdf for each parameter. Off-diagonal elements show the joint distribution of pairs of parameters. Higher probability is represented in red and lower probability in blue (white color for probability under 10^{-4}).

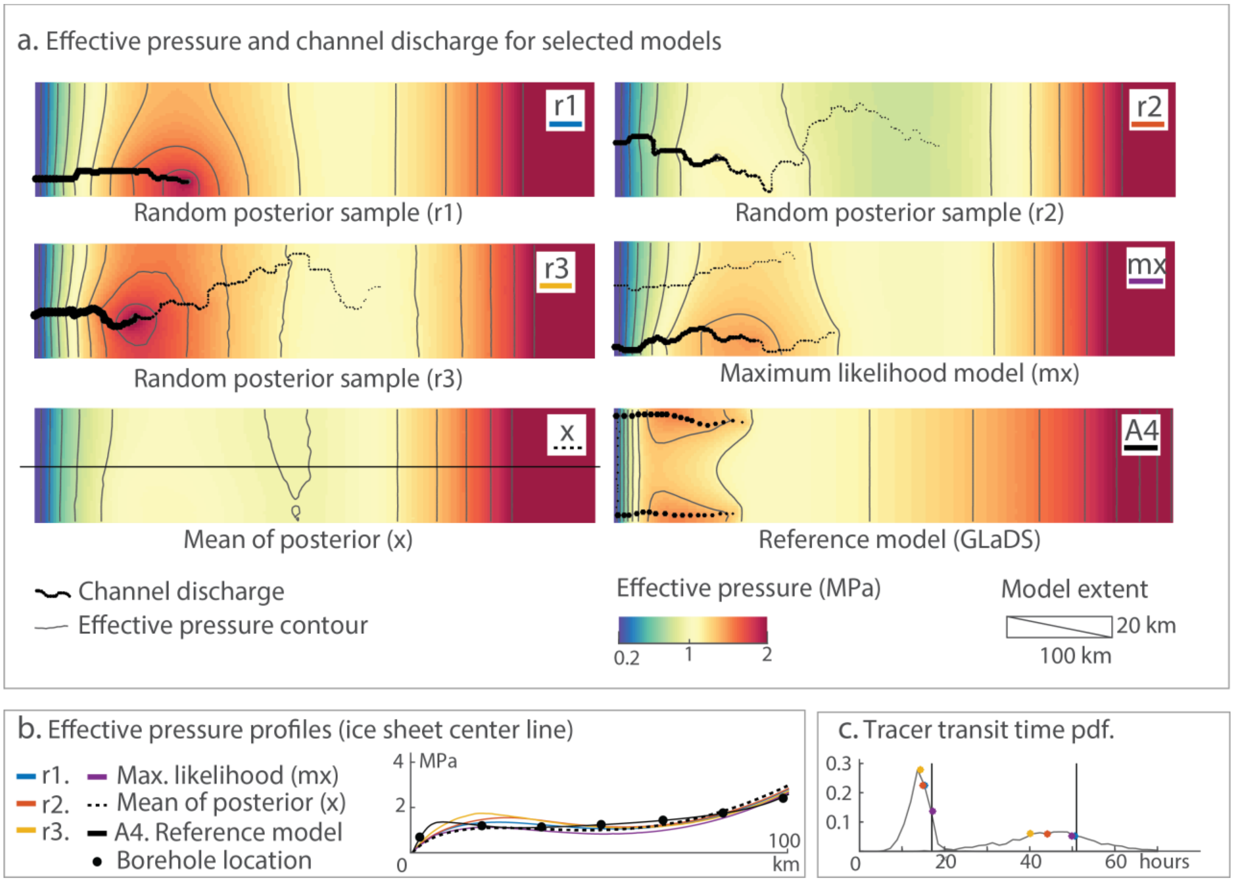

Figure 6. Posterior models for A4. (a) Effective pressure (color scale) and channel discharge over a threshold of 0.5 m^3 s^{-1} (black dots) for a selection of posterior models. Each model represent 100x20 km. The selection includes: three random posterior models (r1, r2 and r3), maximum likelihood model (mx), mean effective pressure (x), and the reference model (A4) from SHMIP. Note that for the mean effective pressure (x) channels are not shown, and profile line for plots in panl b is shown . (b) Effective pressure for the selected models along profiles cutting through the centerline of the ice sheet. (c) Two tracer-transit-time posterior pdf for the two injection points, and its corresponding reference transit time (A4) marked with a vertical black line. The transit times for the selected models are shown in color dots on top of the pdf for each of the injection point.

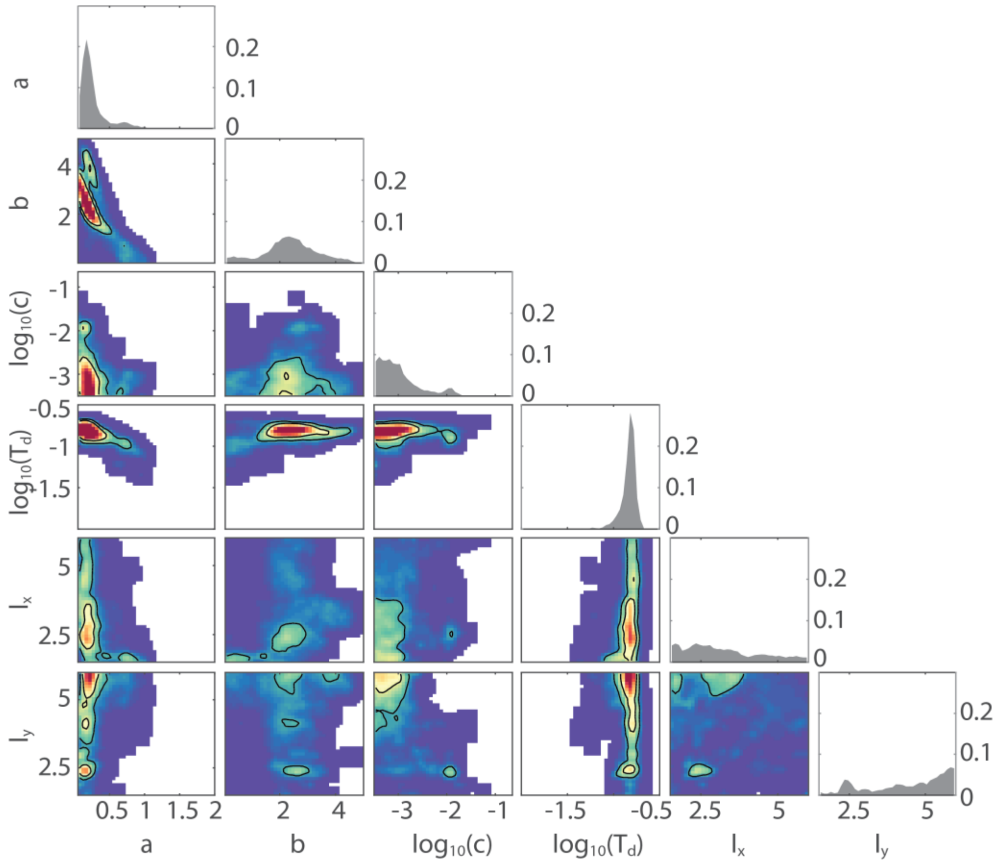

Figure 7. Posterior distributions of the model parameters for case A5. The diagonal shows the posterior pdf for each parameter. Off-diagonal elements are the joint pdf of pairs of parameters. Higher probability is represented in red and lower probability in blue (white color for probability under 10^{-4}).

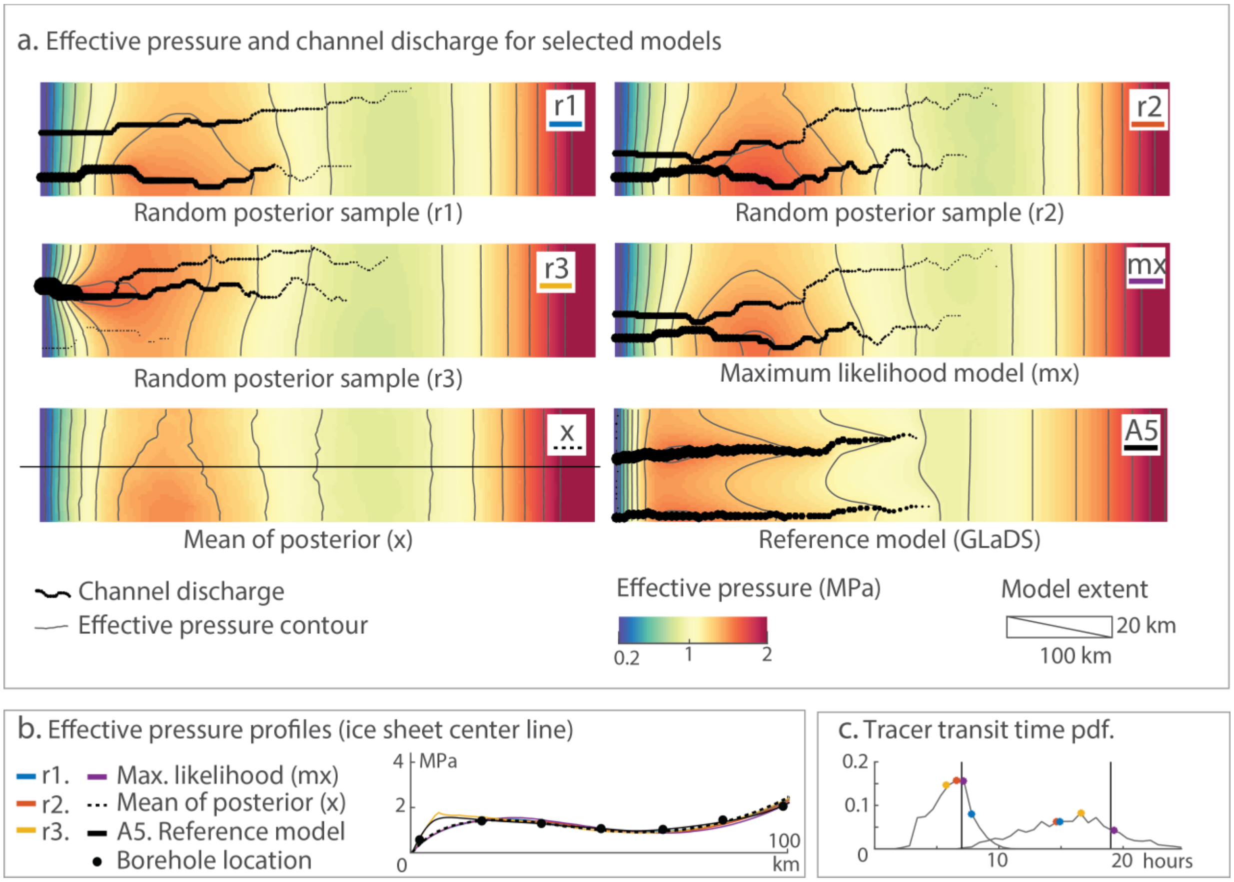

Figure 8. Posterior models for A5. (a) Effective pressure (color scale) and channel discharge over a threshold of 0.5 m^3 s^{-1} (black dots) for a selection of posterior models. Each model represent 100x20 km. The selection includes: three random posterior models (r1, r2 and r3), maximum likelihood model (mx), mean effective pressure (x), and the reference model (A4) from SHMIP. Note that for the mean effective pressure (x) channels are not shown, and profile line for plots in panl b is shown . (b) Effective pressure for the selected models along profiles cutting through the centerline of the ice sheet. (c) Two tracer-transit-time posterior pdf for the two injection points, and its corresponding reference transit time (A5) marked with a vertical black line. The transit times for the selected models are shown in color dots on top of the pdf for each of the injection point.

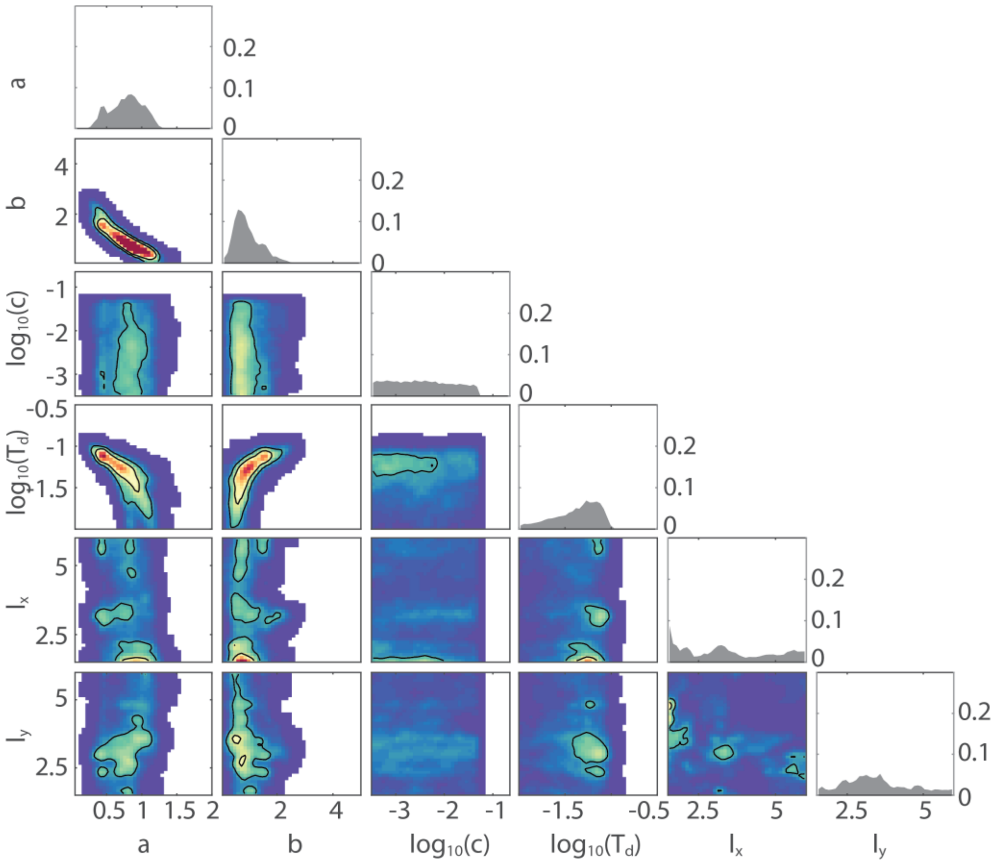

Figure 9. Posterior distributions of the model parameters for case B3. The diagonal shows the posterior pdf for each parameter. Off-diagonal elements are the joint pdf of pairs of parameters. Higher probability is represented in red and lower probability in blue (white color for probability under 10^{-4}).

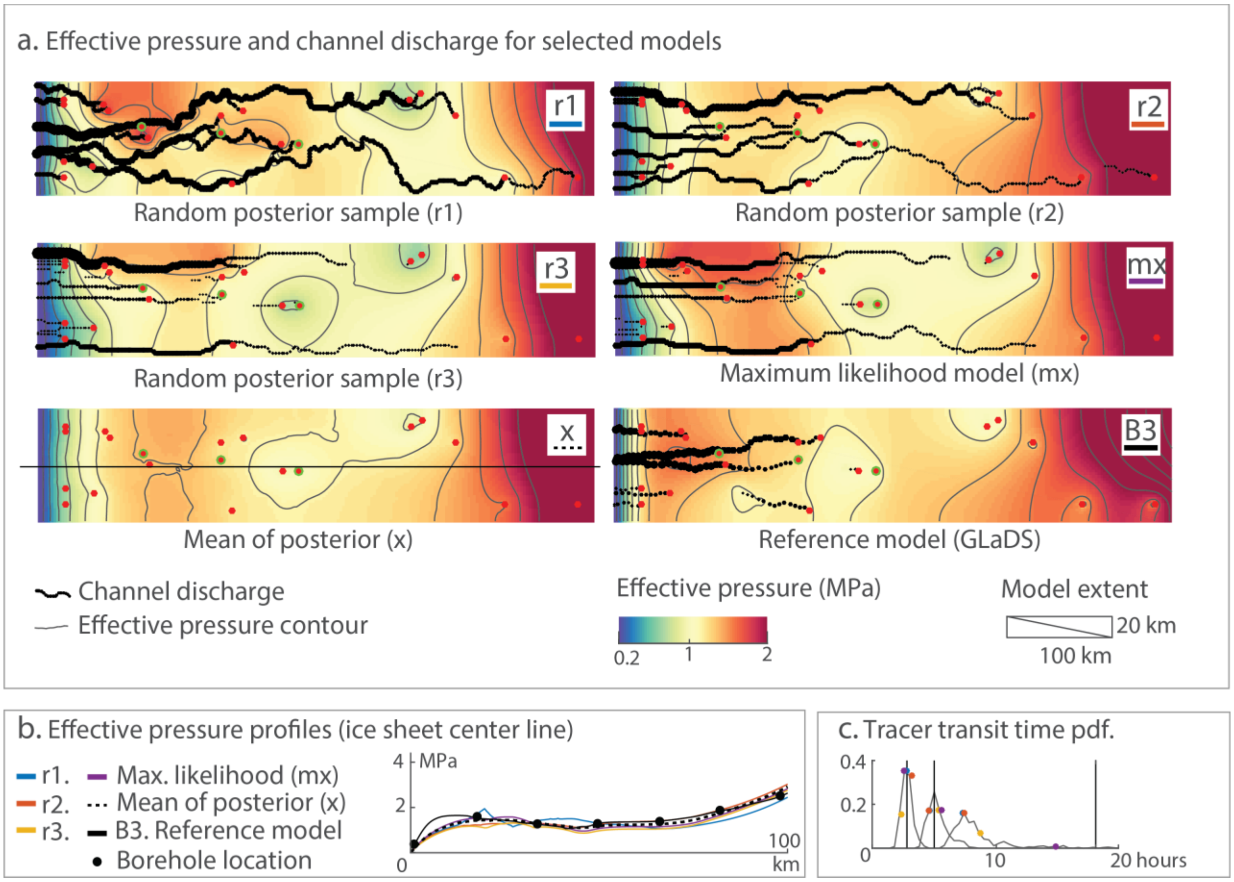

Figure 10. Posterior models for B3. (a) Effective pressure (color scale) and channel discharge over a threshold of 0.5 m3 s-1 (black dots) for a selection of posterior models. Each model represent 100x20 km. The selection includes: three random posterior models (r1, r2 and r3), maximum likelihood model (mx), mean effective pressure (x), and the reference model (A4) from SHMIP. Note that for the mean effective pressure (x) channels are not shown, and profile line for plots in panl b is shown. (b) Effective pressure for the selected models along profiles cutting through the centerline of the ice sheet. (c) Two tracer-transit-time posterior pdf for the two injection points, and its corresponding reference transit time (B3) marked with a vertical black line. The transit times for the selected models are shown in color dots on top of the pdf for each of the injection point.

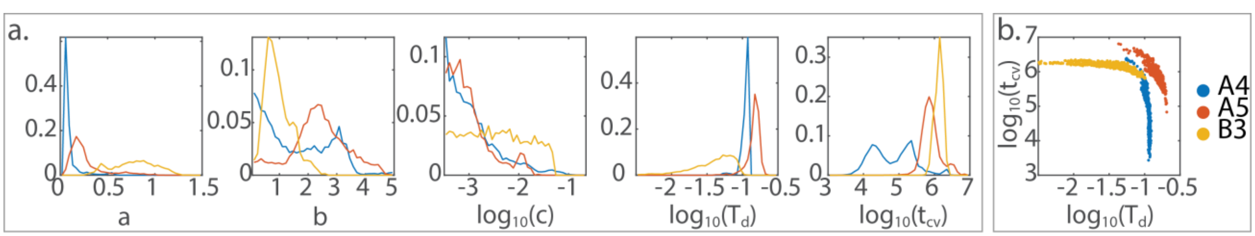

Figure 11. Comparison of the three recharge scenarios A4, A5 and B3. a) Marginal posterior distribution of model parameters plus t_{cv}. b) Plot of T_d v/s t_{cv}.

Figure 1.

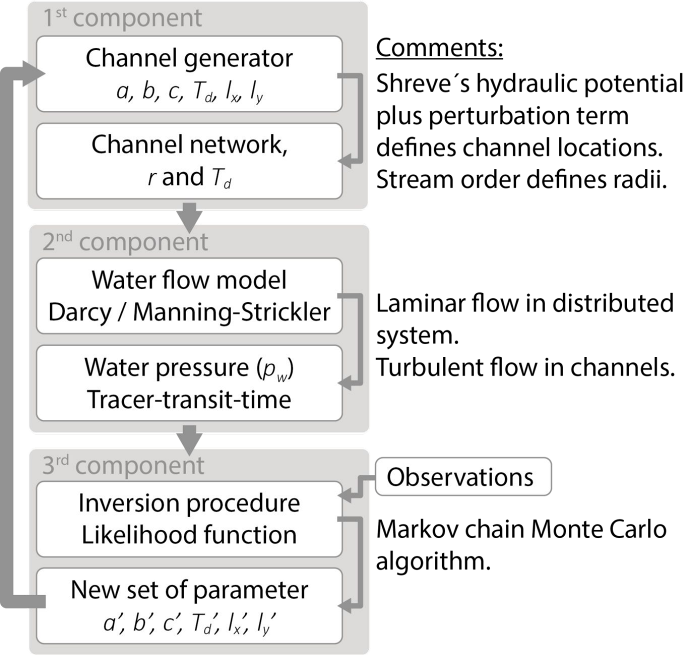
1st component
Channel generator
a, b, c, Td, lx, ly
Channel network,
r and Td
2nd component
Water flow model
Darcy / Manning-Strickler
Water pressure (pw)
Tracer-transit-time
3rd component
Inversion procedure
Likelihood function
New set of parameter
a′, b′, c′, Td′, lx′, ly′
Observations
Comments:
Shreve´s hydraulic potential plus perturbation term defines channel locations.
Stream order defines radii.
Laminar flow in distributed system.
Turbulent flow in channels.
Markov chain Monte Carlo algorithm.

Figure 2.

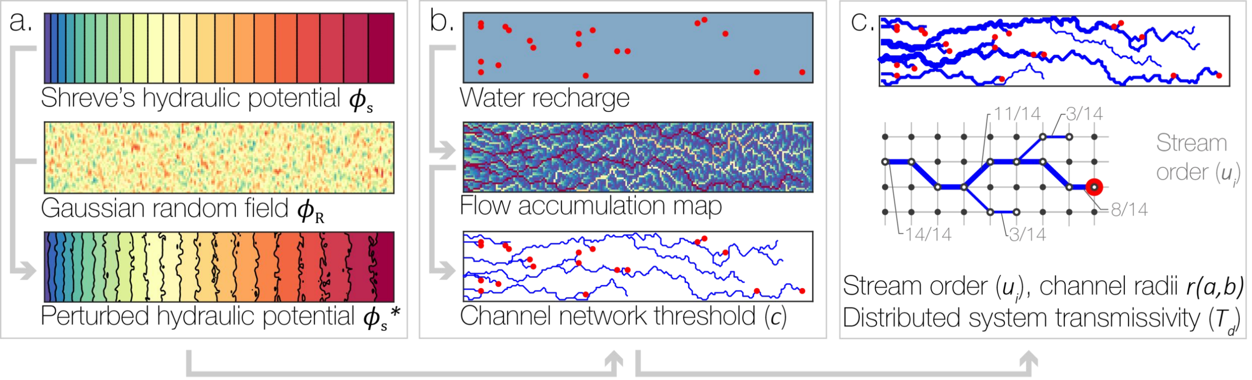

a.
Shreve's hydraulic potential ϕ_s
Gaussian random field ϕ_R
Perturbed hydraulic potential ϕ_s*
b.
Water recharge
Flow accumulation map
Channel network threshold (c)
c.
11/14
3/14
Stream order (u_i)
8/14
14/14
3/14
Stream order (u_i), channel radii $r(a,b)$
Distributed system transmissivity (T_d)

Figure 3.

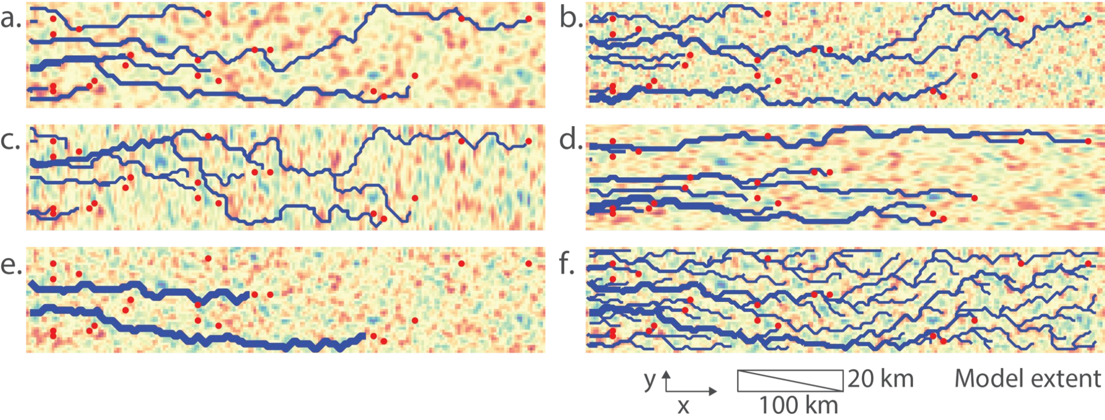
a.
b.
c.
d.
e.
f.
y
x
20 km
100 km
Model extent

Figure 4.

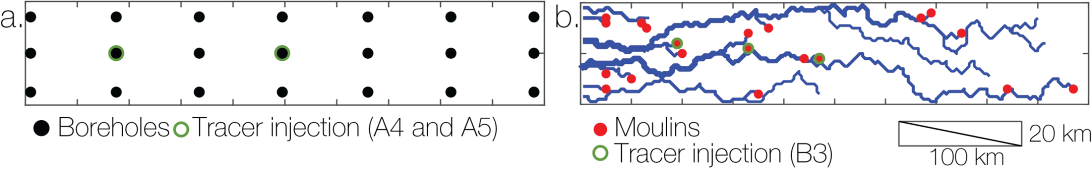
a.
b.
Boreholes
Tracer injection (A4 and A5)
Moulins
Tracer injection (B3)
20 km
100 km

Figure 5.

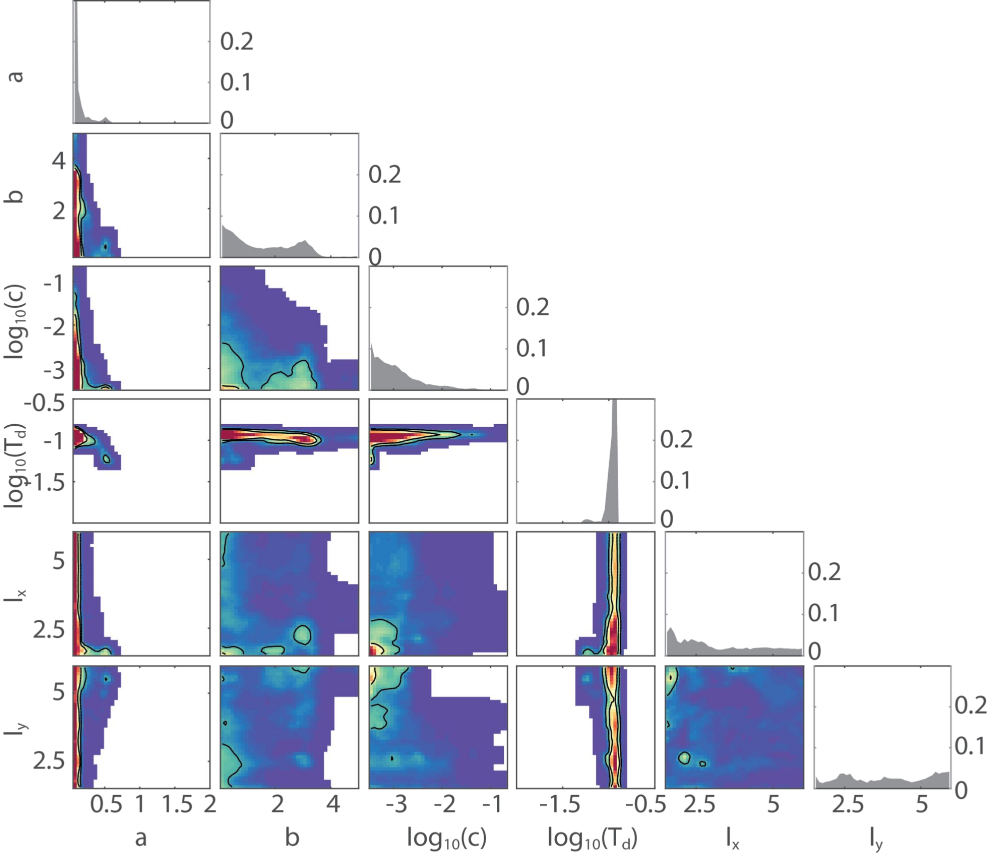

a
b
log10(c)
log10(Td)
lx
ly
0.2
0.1
0
4
2
-1
-2
-3
-0.5
-1
-1.5
5
2.5
0.5
1
1.5
2
2
4
-3
-2
-1
-1.5
-0.5
2.5
5
2.5
5

Figure 6.

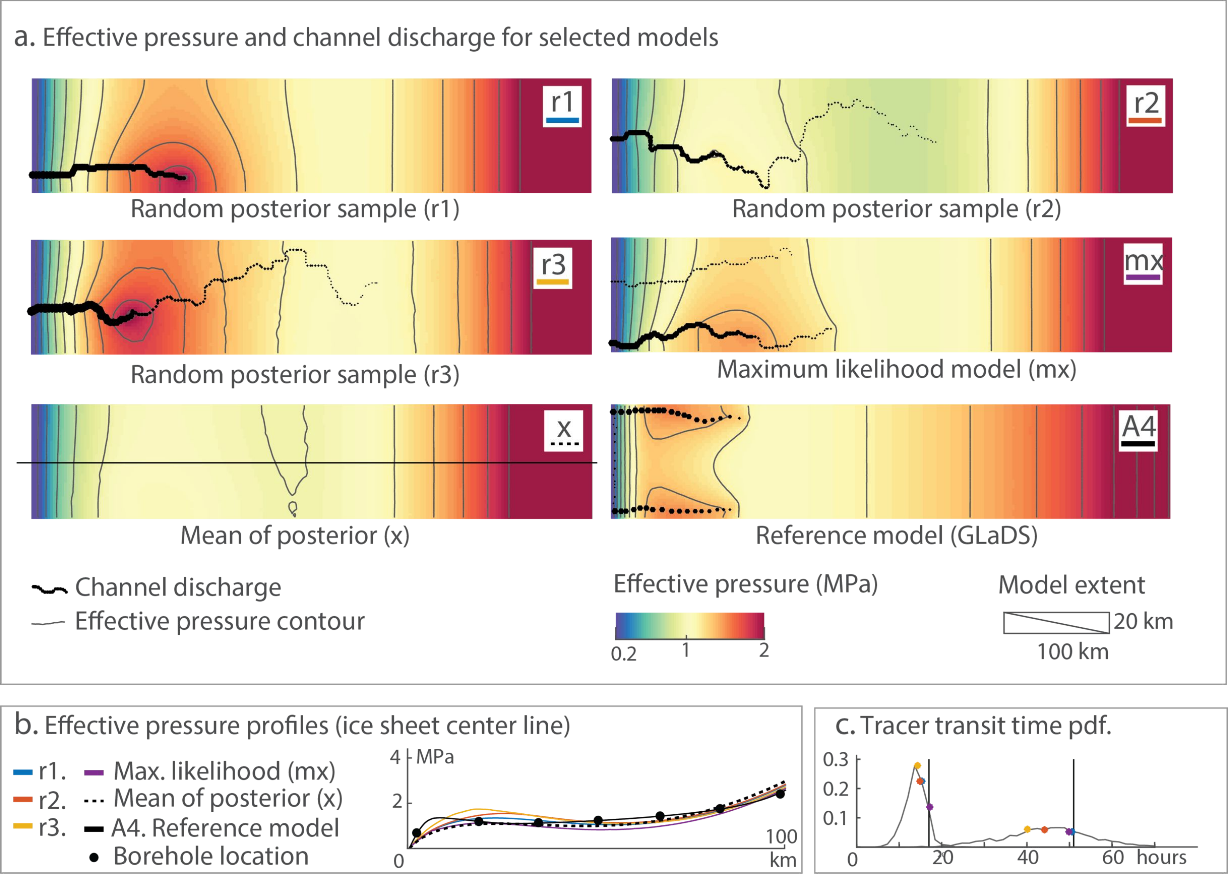

a. Effective pressure and channel discharge for selected models
r1
r2
Random posterior sample (r1)
Random posterior sample (r2)
r3
mx
Random posterior sample (r3)
Maximum likelihood model (mx)
x
A4
Mean of posterior (x)
Reference model (GLaDS)
Channel discharge
Effective pressure contour
Effective pressure (MPa)
0.2
1
2
Model extent
20 km
100 km
b. Effective pressure profiles (ice sheet center line)
r1.
r2.
r3.
Max. likelihood (mx)
Mean of posterior (x)
A4. Reference model
Borehole location
4
MPa
2
0
100
km
c. Tracer transit time pdf.
0.3
0.2
0.1
0
20
40
60
hours

Figure 7.

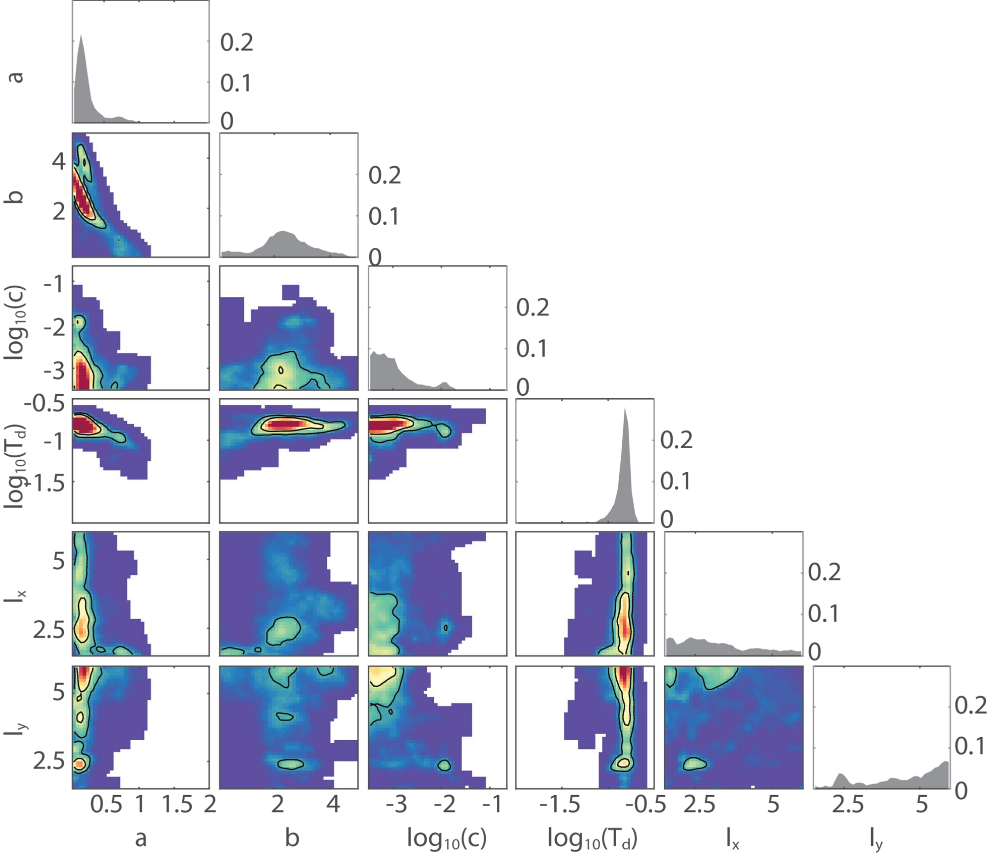
a
b
$\log_{10}(c)$
$\log_{10}(T_d)$
l_x
l_y
0.2
0.1
0
0.5
1
1.5
2
4
-1
-2
-3
-0.5
-1.5
5
2.5

Figure 8.

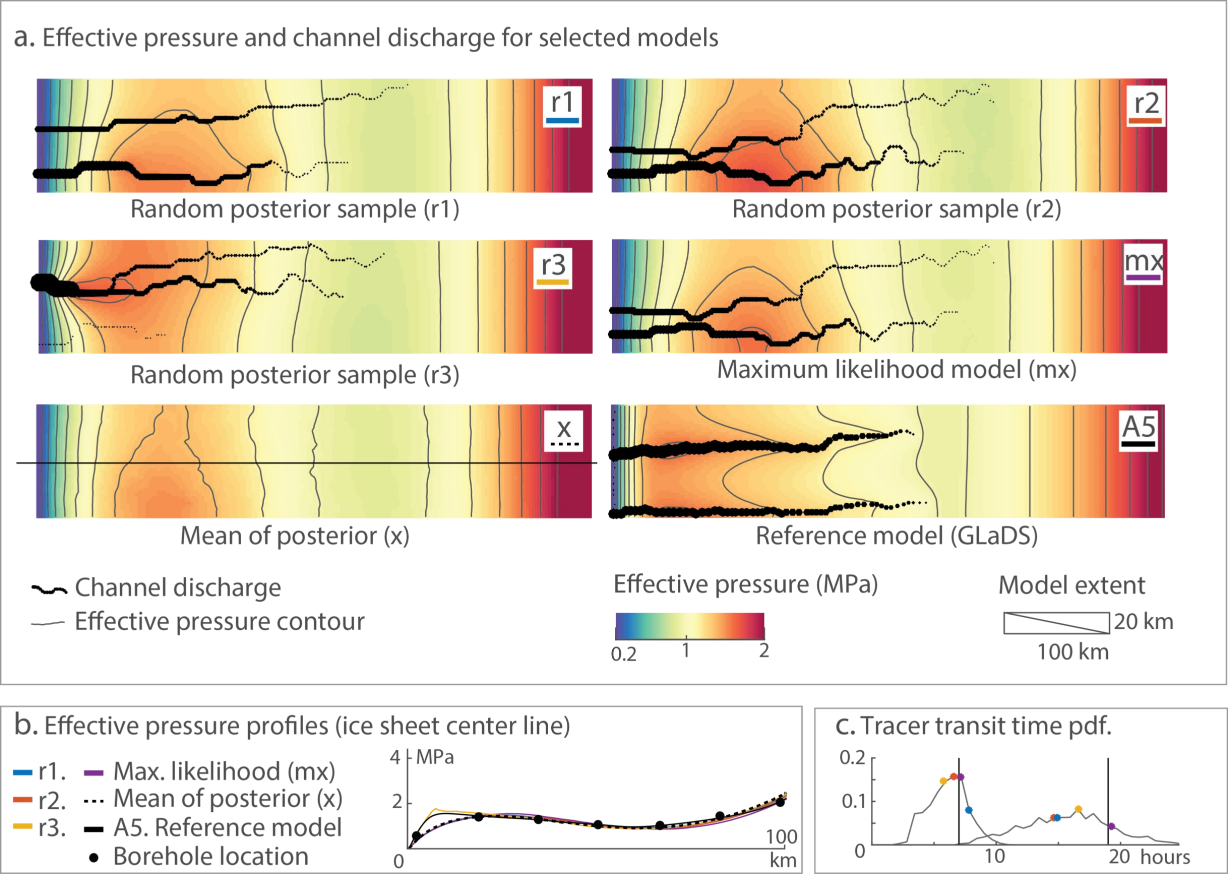

a. Effective pressure and channel discharge for selected models
r1
Random posterior sample (r1)
r2
Random posterior sample (r2)
r3
Random posterior sample (r3)
mx
Maximum likelihood model (mx)
x
Mean of posterior (x)
A5
Reference model (GLaDS)
Channel discharge
Effective pressure contour
Effective pressure (MPa)
0.2
1
2
Model extent
20 km
100 km
b. Effective pressure profiles (ice sheet center line)
r1.
r2.
r3.
Max. likelihood (mx)
Mean of posterior (x)
A5. Reference model
Borehole location
4
MPa
2
0
100
km
c. Tracer transit time pdf.
0.2
0.1
0
10
20
hours

Figure 9.

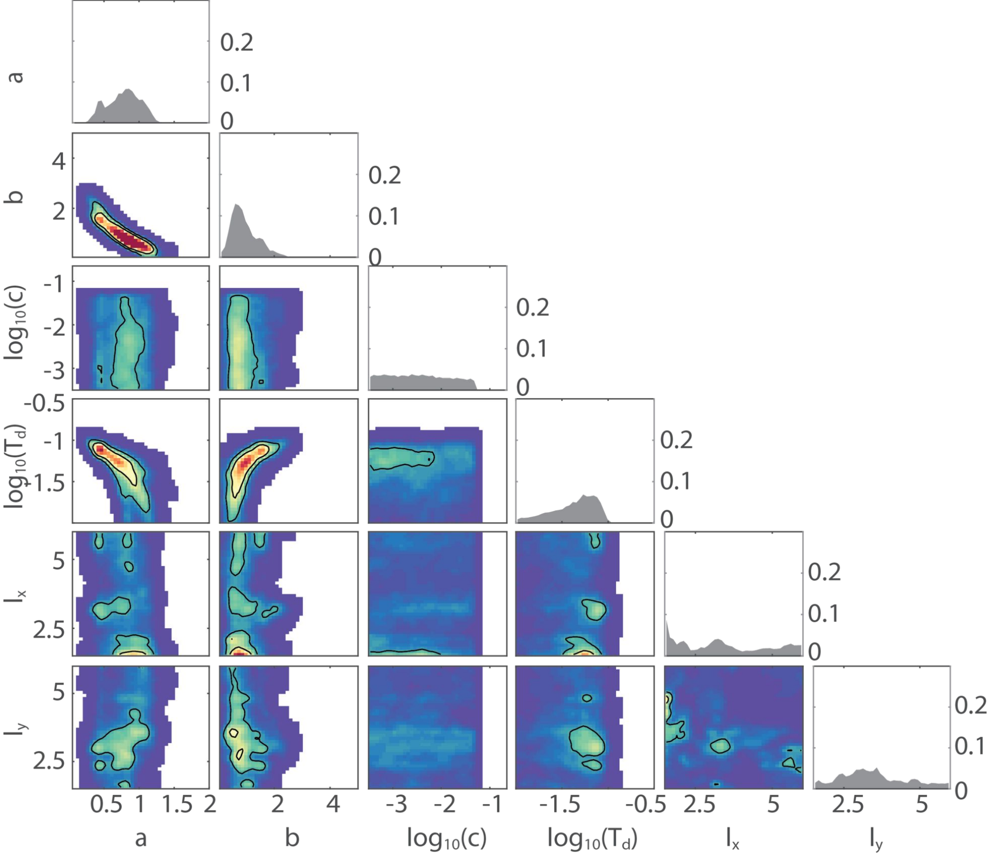
a
b
log10(c)
log10(Td)
lx
ly
0.2
0.1
0
4
2
-1
-2
-3
-0.5
-1.5
5
2.5
0.5
1
1.5
-0.5

Figure 10.

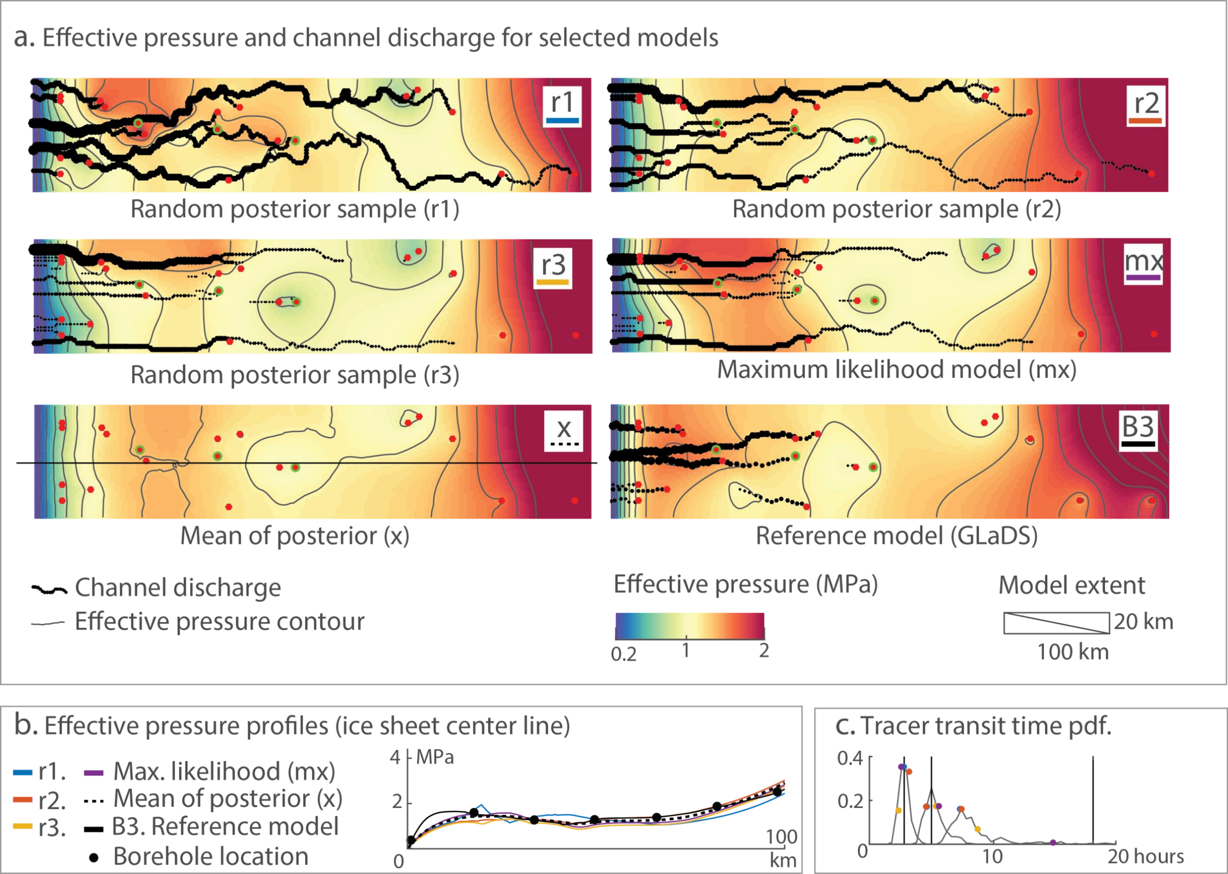
a. Effective pressure and channel discharge for selected models
r1
Random posterior sample (r1)
r2
Random posterior sample (r2)
r3
Random posterior sample (r3)
mx
Maximum likelihood model (mx)
x
Mean of posterior (x)
B3
Reference model (GLaDS)
Channel discharge
Effective pressure contour
Effective pressure (MPa)
0.2
1
2
Model extent
20 km
100 km
b. Effective pressure profiles (ice sheet center line)
r1.
r2.
r3.
Max. likelihood (mx)
Mean of posterior (x)
B3. Reference model
Borehole location
4
MPa
2
0
100
km
c. Tracer transit time pdf.
0.4
0.2
0
10
20 hours

Figure 11.

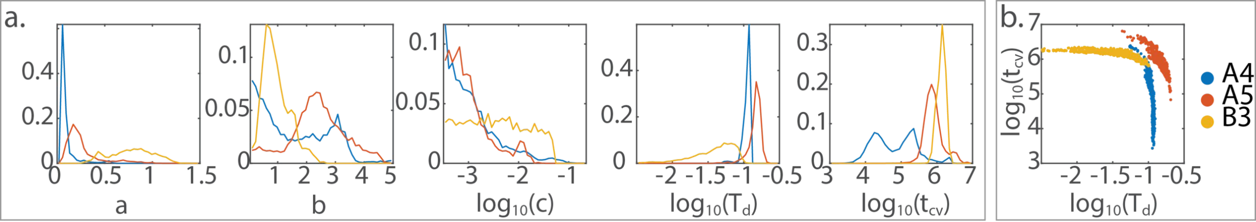

a.
0.4
0.2
0
0
0.5
1
1.5
a
0.1
0.05
0
1
2
3
4
5
b
0.1
0.05
0
-3
-2
-1
$log_{10}(c)$
0.4
0.2
0
-2
-1.5
-1
-0.5
$log_{10}(T_d)$
0.3
0.2
0.1
0
3
4
5
6
7
$log_{10}(t_{cv})$
b.
7
6
5
4
3
-2
-1.5
-1
-0.5
$log_{10}(t_{cv})$
$log_{10}(T_d)$
A4
A5
B3